arXiv:astro-ph/9801137v1 14 Jan 1998

A Spectroscopic Survey of the Galaxy Cluster CL 1358+62 at z=0.328

David Fisher[1]

Kapteyn Astronomical Institute, University of Groningen, Postbus 800, 9700 AV Groningen, The Netherlands

Daniel Fabricant

Harvard-Smithsonian Center for Astrophysics, 60 Garden Street, Cambridge, MA 02138

Marijn Franx and Pieter van Dokkum

Kapteyn Astronomical Institute, University of Groningen, Postbus 800, 9700 AV Groningen, The Netherlands

To appear in the 1998 May 1 Astrophysical Journal

ABSTRACT

We present a spectroscopic survey of the rich, X-ray selected, galaxy cluster CL 1358+6245 at z=0.328. When our 173 new multi-slit spectra of cluster galaxies are combined with data from the literature, we produce a catalog of 232 cluster members in a region $10' \times 11'$ (3.5 Mpc $\times$ 3.8 Mpc) surrounding the brightest cluster galaxy. These data are used to study the structure and dynamics of the cluster and to examine the radial and velocity distributions as a function of spectral type. We classify the spectral types of the cluster members according to the strengths of the Balmer absorption lines (Hδ, Hγ, and Hβ) and the [OII] 3727 Å emission line.

We derive a mean redshift of z=0.3283$\pm$0.0003, and a velocity dispersion of 1027^{+51}_{-45} km s^{-1} for the 232 cluster members. However, the

[1]Current address: Universität Hamburg, Hamburger Sternwarte, Gojenbergsweg 112, 21029 Hamburg, Germany

cluster velocity distribution is non-Gaussian and we identify at least two subgroups with 10-20 members and dispersions <400 km s^{-1}. The fraction of spectroscopically active galaxies (poststarburst and emission-line) in the core of the velocity distribution (within 0.6 σ of the mean cluster velocity) is 16±4%, rising to 32±7% for galaxies in the tails of the velocity distribution (2.0 σ from the mean cluster velocity). In total, the cluster is composed of 19±3% emission-line and 5±1% poststarburst galaxies. The velocity dispersion of the poststarburst galaxies is close to $2^{1/2}$ times that of the absorption-line galaxies, consistent with free-fall accretion of the poststarburst galaxies.

The changing mix of galaxy spectral types as a function of local galaxy density (or distance from the cluster center) in CL 1358+62 is similar to what is observed in nearby rich clusters. The percentage of emission-line galaxies increases steadily with radius from 9±3% within a radius of $r_{\rm p}$<0.7 Mpc, to 41±9% in our outermost radial bin at ∼1.7 Mpc. The percentage of absorption-line galaxies falls from 84±9% to 59±11% over the same radial intervals. These results are consistent with the idea that the cluster grows through the accretion of late-type field galaxies, a fraction of which are transformed into poststarburst galaxies during the accretion event.

Our high signal-to-noise spectra of the "E+A" galaxies allow a detailed comparison with spectra of nearby merging and strongly interacting galaxy systems. We find that nearby mergers have stronger [OII] 3727 Å emission ([OII] EW > 5 Å) than that observed for our "E+A" galaxies. This implies either that the "E+A"galaxies in CL 1358+62 were not formed through major mergers, or that if they were formed via merging, their gas-supply was then quickly depleted, possibly by the ICM.

Subject headings: galaxies: clusters: individual (CL 1358+6245) — galaxies: distances and redshifts — galaxies: elliptical and lenticular, cD — galaxies: evolution — galaxies: kinematics and dynamics

1. Introduction

CL 1358+6245 is one of the richest medium redshift galaxy clusters known (see Luppino et al. 1991). The cluster was originally selected from the *Einstein* Medium Sensitivity Survey (Gioia et al. 1990, Gioia & Luppino 1994) by Fabricant, McClintock & Bautz (1991, hereafter FMB) on the basis of its large X-ray luminosity: $L_x \sim 7\times 10^{44}$ ergs s^{-1} (0.2-4.5 keV). The FMB study used X-ray selection to avoid possible biases associated with optical selection (see Koo 1988), although they established that the galaxy populations of X-ray selected clusters at intermediate redshifts are similar to those in optically selected clusters.

Here, we present a much expanded spectroscopic study of the cluster based on new data obtained at the William Herschel Telescope (WHT) with the Low Dispersion Survey Spectrograph (LDSS-2). We obtained redshifts of 328 additional galaxies, 173 of which are cluster members. The spectra are of sufficient quality to determine the main characteristics of the stellar populations in the cluster galaxies from line strength measurements of emission and absorption features. We use the spectroscopic data to explore the cluster dynamics and the evolution of its galaxy population. The work reported here is part of a larger study of the evolution of X-ray selected clusters at increasing redshift, combining ground-based spectroscopy and photometry with HST WFPC2 images.

There is now substantial evidence that galaxy populations in distant clusters differ from the populations in nearby clusters. Butcher & Oemler (1978, 1984) demonstrated that the fraction of blue galaxies in clusters increases from about 3% in nearby clusters to 25% at $z\sim 0.5$. Spectra of these blue galaxies revealed both emission-line galaxies, and surprisingly, poststarburst galaxies with strong Balmer absorption lines (Dressler & Gunn 1983). The poststarburst galaxies (often called "E+A" galaxies) are believed to have experienced a burst of star formation that ended approximately 1 Gyr before the epoch of observation.

Previous studies have suggested that the emission-line and poststarburst galaxies are found preferentially in the outer regions of clusters (e.g., Couch & Sharples 1987; FMB; Colless & Dunn 1996; Abraham et al. 1996). A goal of our current program is to map the distribution of the spectroscopically active galaxies to help constrain their evolutionary history. HST studies will reveal the morphology of these distant galaxies, and will add important evolutionary constraints, but ground-based spectroscopy of the type we report here remains essential to our progress in this field.

In addition to studying the evolution of cluster galaxies, we wish to address the evolution of clusters as dynamical systems. Simulations (reviewed in Evrard 1993) suggest that in bottom-up hierarchical clustering models, many generations of subcluster merging are likely to have occurred in rich clusters by the present epoch. Furthermore, these models predict that the accretion of galaxies into the cluster and the frequency of localized velocity structures should increase as a function of lookback time (Gunn & Gott 1972). Large numbers of redshifts are needed to determine the degree of dynamical mixing within a cluster and observations at the current epoch have yielded important tests of these models of cluster formation. Observations at intermediate redshift have only recently become available (e.g., Carlberg 1994) and are of partic-

ular importance because they can be used to directly search for dynamical evolution.

The paper is organized as follows. First, we describe the photometric catalog (§2) from which we selected objects for spectroscopy. The design of the multislit aperture masks used to obtain the spectroscopy, spectroscopic reduction techniques, and determination of radial velocities are discussed in §3. The spectroscopic catalog is presented in §4 including a description of the completeness of the spectroscopic sample and the definition of the line strength indices used to classify the galaxy spectra. In §5, we discuss the spectral types observed in our galaxy sample. The changing mix of spectral types as a function of local galaxy density or distance from the cluster center and the dependence of the galaxy velocity distribution on spectral type are discussed in §6. Our search for subclustering is discussed in §7. A summary of our findings is presented in Section §8.

2. Photometric Catalog

In 1992 we obtained V and R images of CL 1358+62 at the Fred L. Whipple Observatory's 1.2-m telescope, covering the central $10' \times 11'$ portion of the cluster. Multiple exposures in V and R were obtained with small spatial offsets between exposures. The observations consist of three 900 sec R exposures and five 1200 sec V exposures. We used a Ford 2048×2048 pixel CCD with a scale of $0.325''$ pixel^{-1}. The seeing was $1.2''$ during the run and conditions were not photometric so we normalized to the FMB zeropoints for V and R. The images were reduced in the standard fashion to create a master frame for each run and each filter. We used the Faint Object Classification and Analysis System (Jarvis & Tyson 1981; Valdes 1982a,b, hereafter FOCAS) to extract aperture photometry, positions and object classifications (galaxy, star, defect). We used 10 pixel diameter ($3.25''$) apertures for the data, close to the $3.3''$ apertures that FMB used. At the distance of CL 1358+62, $3.3''$ corresponds to 19 kpc (for consistency with FMB we assume H_0=50 km s^{-1} Mpc^{-1} and q_0=1/2 throughout). The expected reddening towards CL 1358+62 is small [E($B-V$)=0.01] and so no corrections have been made for Galactic reddening (Burstein & Heiles 1984). The photometric catalog resulting from these images was used to select objects for our spectroscopic runs.

In 1994, we obtained additional V and R images with the WHT LDSS-2 spectrograph (operated as a focal reducer) that cover an approximately circular region of $8'$ diameter slightly offset from the cluster center. The LDSS-2 detector was a 1024×1024 Tektronix CCD with a scale of $0.592''$ pixel^{-1}. The WHT observations consist of seven 300 sec R exposures and two 300 sec V exposures. The seeing was $1.6''$ during the run and flux standards were not observed so we extracted counts in $\sim 3.3''$ apertures and normalized to the FMB zeropoints. The LDSS-2 images are rather coarsely sampled, but are deeper than the Whipple 1.2-m images. Aperture photometry in 6 pixel diameter ($3.55''$) apertures was extracted from the reduced images with the FOCAS package. The $V-R$ object colors presented here are drawn from this WHT catalog.

We can estimate the completeness of the WHT photometry by examining the distribution of galaxy counts as a function of magnitude well away from the cluster core. We find that log N$\propto R^{0.3}$ for $20< R <23.5$. The counts in the $23.5< R <24$ bin fall 20% below this re-

lation and the counts in the 24< R <24.5 are over a factor of two below the relation. We therefore expect that the WHT photometry is substantially complete to $R \sim 23.5$. There are two areas of local incompleteness surrounding two stars that saturated the CCD: one of radius $\sim 50''$ at $13^h\ 58^m\ 21.0^s$, $62^\circ\ 50'\ 23''$ (1950) and one of radius $\sim 20''$ at $13^h\ 58^m\ 52.1^s$, $62^\circ\ 44'\ 56''$ (1950).

A multi-color mosaic of HST WFPC2 images of CL 1358 has been obtained. This mosaic offers an unprecedented high resolution view of a large area of a cluster at intermediate redshift. We refer the reader to a companion paper (van Dokkum et al. 1997), which uses these HST images to study the galaxy morphologies and color-magnitude relation in the cluster.

3. WHT Spectroscopy

The new spectra were obtained during two observing runs with the LDSS-2 spectrograph at the WHT: a 3 night run in April 1994 and a 5 night run in June 1996. The LDSS-2 is a multi-slit spectrograph with an $11' \times 11'$ field of view that is mounted at the Cassegrain focus of the WHT (see Allington-Smith et al. 1994). The aperture plates used for our two runs contained slitlets $1.5''$ wide and $\sim 15''$ long. The masks used for the first WHT run each contained $\sim$30 slitlets; the masks for the second run each contained $\sim$50 slitlets.

3.1. Aperture Plate Layout

The design of aperture plates for the MMT is described in FMB. FMB obtained spectra for 70 galaxies within R_{30} ($\sim 2'$) of the dominant central cluster galaxy, yielding 59 redshifts of cluster members.

For the first WHT spectroscopic run galaxies with $R \leq 21$ were given highest priority. Nine masks were designed with an optimizer which attempted to maximize the assignment of high priority galaxies. Fainter galaxies were assigned priorities proportional to their magnitude and were used to fill the remaining spaces in the masks. Observing time was available to expose six of the nine masks, yielding spectra of 127 high priority galaxies and 35 lower priority galaxies.

Similar galaxy priorities were assigned for the second WHT run except that objects falling outside the HST mosaic ($8' \times 8'$) were assigned the lowest priority independent of their magnitude. The automated selection procedure was used to design nine masks and all nine aperture plates were exposed. Spectra for 42 galaxies with $R \leq 21$ and 172 fainter galaxies were obtained.

3.2. Instrument Configuration

For the 1994 WHT run and the first 2 nights of the 1996 WHT run, we used a Tektronix 1024×1024 CCD with 24 μm pixels with a pixel scale of $0.59''$ pixel^{-1}. For the last 3 nights of the 1996 WHT run we used a Loral 2048×2048 CCD with 15 μm pixels and a spatial scale of $0.37''$ pixel^{-1}. The read out noise and gain of the Tektronic chip was 4.4 e$^-$ and 1.2 e$^-$/ADU respectively, while that of the Loral chip was 6 e$^-$ and 0.8 e$^-$/ADU. Exposure times were 4×1800 sec for the Tektronic chip and 3×2400 sec for the Loral with each aperture plate.

The 300 line mm^{-1} grism blazed at 5000 Å was used for all observations, providing a resolution of 13 Å FWHM with the aperture plates. The dispersion was 5.3 Å pixel^{-1} with the Tektronix CCD and 3.3 Å pixel^{-1} with the Loral CCD. The wavelength coverage depends on the layout of the aperture mask but

typically includes the range 3500-8500 Å. This wide wavelength coverage is beneficial for the identification of field galaxies to $z \sim 1$. In the cluster rest frame our coverage extends from well below the [OII] 3727 Å emission line to well beyond the Mg I triplet at 5175 Å.

3.3. Data Reduction and Analysis

Data reduction for the 1994 WHT run was carried out with IRAF while reduction of the 1996 WHT run was carried out with VISTA (Lauer, Stover, & Terndrup 1983). In brief, the processing steps for each CCD exposure were: bias subtraction, flat-fielding, wavelength calibration and geometrical rectification. Following this, cosmic ray events were removed and the individual spectra were extracted. One-dimensional spectra, binned logarithmically in the wavelength direction, were the final product of these procedures. Flux standards were not obtained, so flux calibration was not attempted.

The identification and removal of cosmic ray events is a critical step in the reduction process because they can be confused with emission lines. We generated a cosmic ray map for each frame by subtracting a median of the multiple exposures of each mask from the individual exposures and setting to zero all pixels less than 5σ above the median level. Following subtraction of the cosmic ray map, each frame was visually inspected for remaining deviant pixels before combining it with the other exposures. Straight medians of the individual exposures were created to aid the separation of cosmic ray events from emission lines in ambiguous cases.

The major difference between the reduction procedures for the two runs was that the wavelength calibration was performed after extraction of one dimensional spectra for the 1994 data, while it was performed prior to extraction for the 1996 data. The results of both procedures are essentially indistinguishable. CuAr spectra were obtained with each aperture plate to determine the wavelength solutions for each slitlet. Wavelength calibration for each slitlet was performed using a fifth-order polynomial fit to ∼15-20 arc spectrum lines. The rms residuals from these fits are $\lesssim$0.2 Å. As a final step in the wavelength calibration the position of the 5577 Å night skyline was measured and used to correct for any offset to the wavelength solution caused by relative shifts between the arc and galaxy exposures. This correction was usually of order 1 Å or less.

We estimate that residual errors in the final wavelength-calibrated and line curvature-corrected spectra are present at the level of $\lesssim$0.5 Å, as determined from measurements of the positions of prominent spectral features. By themselves, these errors can result in redshift uncertainties of ∼28 km s^{-1} or $\varepsilon(z) \approx 0.00009$. We discuss our estimated external errors below.

3.4. Determination of Redshifts

Redshifts were derived from either the absorption lines using a cross-correlation technique (Tonry & Davis 1979) or directly from the emission lines. These techniques are similar to those used by FMB. The subsections below describe the details of the derivations of radial velocities for the cluster members.

3.4.1. Absorption Line Redshifts

Redshifts were determined by cross-correlating template spectra with cluster galaxy spectra for the 188 (177 red absorption-line galaxies + 11 poststarburst galaxies) galaxies with WHT spectra dominated by stellar absorp-

tion features. Two high signal-to-noise template spectra were used: a spectrum of the central regions of the early-type galaxy NGC 7331 and a spectrum of a poststarburst galaxy in the cluster (number 209). A semiautomated procedure was developed to cross-correlate the object spectra with the templates using the cross-correlation routine, XCSAO. XCSAO (Kurtz et al. 1992) is part of the RVSAO package for the IRAF environment. The velocities and their errors are returned by the XCSAO software. Each object spectrum was cross-correlated with the each of the two templates within the 3530−5110 Å rest frame wavelength range.

The 14 galaxies from the FMB study which were reobserved with the WHT allow us to estimate the external errors. The RMS velocity difference between the FMB and the new WHT results is ∼100 km s^{-1}, yielding an estimated uncertainty of ∼70 km s^{-1} for an individual measurement if the MMT and WHT errors are equal. In fact, the WHT have higher resolution and (in general) higher signal-to-noise. We therefore assign an error of 60 km s^{-1} to the highest quality WHT spectra and 80 km s^{-1} to the highest quality MMT spectra. We estimate that the errors in the lower quality MMT spectra are 120 km s^{-1}. This comparison of the FMB and WHT redshifts suggests that FMB significantly overestimated their errors.

3.4.2. Emission Line Redshifts

The sky subtracted two-dimensional slitlet frames and one-dimensional object spectra were inspected for emission features and they were detected in 44 galaxies. For these galaxies redshifts were often determined solely from the [OII] 3727 Å, although in some cases additional lines (usually [OIII] 5007 Å and Hβ) were present. The emission line positions and their associated errors were measured by fitting a Gaussian profile with the IRAF SPLOT task.

Eight of the galaxy spectra in our catalog have redshifts determined from both absorption and emission lines. The largest difference between the emission-line and absorption-line derived radial velocities for the eight galaxies is 143 km s^{-1}. The RMS velocity difference for the eight galaxies is 53 km s^{-1}, which implies an internal error in the WHT velocity determinations of ∼40 km s^{-1}.

4. Spectroscopic Catalog

Cluster membership was defined to include all galaxies within the redshift interval $0.31461 < z < 0.34201$. This corresponds to the $4\sigma_{\rm cl}$ boundary around the cluster mean. The nearest galaxies in redshift space outside these boundaries are at $+4.5\sigma_{\rm cl}$ and $+5.9\sigma_{\rm cl}$. Both these galaxies are also at large projected distance from the cluster center (260″, 1.5 Mpc and 310″, 1.8 Mpc respectively) and are therefore not likely to be cluster members. Table 1 presents our results for the full sample of 232 cluster members including the FMB results. The galaxy (x,y) positions are given with respect to the brightest cluster galaxy (number 375 at R.A. (1950) $13^h58^m20^s.7$ DEC (1950) $62°45'33''$) with positive x towards the West and positive y to the North.

4.1. Completeness

The three major selection effects which could influence the completeness of our survey are uneven spatial sampling, a magnitude bias, and a color or spectral type bias. A spatial sampling bias could result from an uneven distribution of the aperture plate

slitlets. A magnitude bias naturally arises because redshifts are more difficult to measure for faint galaxies. Completeness may depend on the galaxy colors or spectral types because redshifts are generally easier to measure for galaxies with emission lines. (see, e.g., Yee, Ellingson, & Carlberg 1996).

The spatial distribution of all galaxies from the 1.2 m photometric catalog with $R \leq 21$ is plotted in Figure 1. The subset of galaxies for which we have measured redshifts have been marked. The region covered by the spectroscopy is outlined, i.e., $-5' \lesssim x \lesssim +5'$ and $-6' \lesssim y \lesssim +5'$. Of the 226 galaxies in this field with R$\leq$21, we have obtained redshifts for 189 (84%). There are 154 galaxies with $R \leq 21$ in the inner half of the spectroscopic field (by area), and we obtained redshifts for 138 (90%). The outer half of our field (by area) contains 72 galaxies for which we acquired 51 redshifts (71%).

The completeness of our spectroscopic sample as a function of magnitude is shown in Figure 2. Fig. 2 plots the ratio of the number of galaxies (including cluster and field galaxies) with measured redshifts to the total number of galaxies in the photometric catalog in a magnitude bin centered on each galaxy. We used a magnitude bin of ± 0.50 for $R \leq 20$ and a magnitude bin of ± 0.25 for fainter objects. Those objects brighter than the brightest cluster galaxy (at R=19.09) are foreground galaxies. Fig. 2 indicates that our spectroscopic sample is >80% complete for $R \leq 21$ and drops steeply to 20% completeness at R$\sim$22.

To check if our ability to measure redshifts depends on color, we divided our sample into red ($V-R$>0.75) and blue ($V-R$<0.75) samples. We find that we are 100% successful in determining redshifts for objects with R<21, and at R$\sim$23 the success ratio drops to 50%. The success ratio does not depend strongly on color for R<23.5. At fainter magnitudes the statistics are poor: we detect 1 of 6 targeted blue galaxies and 2 of 4 targeted red galaxies. We conclude that any color biases (and by inference spectral type biases) in our catalog are minor.

4.2. Absorption and Emission Line Strength Measurements

The resolution and limited signal-to-noise ratio of our spectra prevent us from studying subtle spectral features. Therefore, we concentrate on the most prominent spectral lines that measure star formation activity: the Balmer absorption lines (Hδ, Hγ, and Hβ), and the [OII] 3727 Å emission line.

Three wavelength regions need to be defined in order to measure a spectral index: an interval covering the feature of interest, and a pair of continuum bandpasses on either side of the feature. The strength of each spectral index is a measure of the flux in the central bandpass compared to a continuum level set by the sidebands. The indices we measure here are tabulated as equivalent widths in Å. These equivalent width (EW) measurements using the observed spectra are corrected into the rest frame by dividing by $(1+z)$.

The line strength indices that we use are defined in Table 2. The Hδ, Hγ, and Hβ indices are based on Jones & Worthey (1995) but we have broadened the continuum sidebands and moved them further from the central bandpass. We have moved the Jones & Worthey Balmer sidebands because their sidebands overlap the absorption lines for poststarburst galaxies. Figure 3 shows the spectrum of our strongest poststarburst galaxy (number 243) with our Balmer line index

definitions overlaid. The Jones & Worthy Balmer indices are located ∼20-30 Å closer to the feature bandpasses on both sides, and fall inside the features being measured. We have, however, used the wavelength regions of Jones & Worthey for the central bandpasses because 95% of the cluster galaxies are *not* poststarburst and wider feature bandpasses for these galaxies would include unwanted regions of the spectrum in addition to the Balmer lines. Conversely, for the strongest poststarburst galaxies, the Jones & Worthey central bandpasses are too narrow to include the full widths of the Balmer lines, leading to up to 30% underestimates of the true equivalent widths. As an example, the poststarburst galaxy shown in Fig. 3 has an average balmer line strength of 9.1 Å in our system whereas a measurement including the full line widths gives 12.0 Å. For the purposes of spectral classifications our system provides a rigorous means of measuring the Balmer line strengths for the wide range of galaxy spectra found in CL 1358+62.

We also define our own [OII] emission-line index which we give in Table 2. The equivalent widths that we measure for all galaxies are given in Table 1. Errors are calculated by measuring the noise in the continuum sidebands and scaling this to the indices themselves.

5. Galaxy Spectral Types

5.1. Definition of Spectral Types

Our spectra display a wide variety of nebular emission line and absorption line strengths. The galaxy spectra can be sorted into spectral classes which are directly related to the star formation histories of the galaxies. We have divided the cluster galaxy spectra into three spectral types: (1) a population displaying the normal absorption features of elliptical and S0 galaxies and no emission lines, (2) poststarburst galaxies with strong Balmer absorption lines and no emission features, and (3) galaxies with emission lines, a broad classification which includes blue galaxies as well as red galaxies with absorption-line spectra and weak emission features.

The dominant spectral type in our catalog corresponds to the first of these types: spectra of red galaxies that likely have elliptical and S0 morphologies. Of the 232 cluster members, 177 (76%) have pure absorption-line galaxy spectra dominated by the 4000 Å break. These galaxies are labeled "abs" in Table 1. The lower right panel of Figure 4 shows a typical absorption-line spectrum (galaxy number 353).

The spectra of poststarburst galaxies can be modeled as the combination of an old stellar population whose light is dominated by K giant stars and a young population of hot, strong Balmer-lined A stars (Dressler & Gunn 1983; Couch & Sharples 1987). We have defined a sample of 11 poststarburst galaxies which have average Balmer absorption line strengths, (Hδ+Hγ+Hβ)/3, greater than 4.0 Å and [OII] 3727 Å emission less than 5 Å. The Balmer line strength measurements are required to be significant at least at the 1 σ level. The 11 poststarburst galaxies are labeled "e+a" in Table 1.

Histograms of average Balmer line strength for all 232 cluster members and for the galaxies without [OII] 3727Å emission are plotted in Figure 5. Our cutoff for poststarburst classification is justified in the lower panel of Figure 6, which is a plot of average Balmer line strength versus galaxy color. The poststarburst galaxies can be clearly dis-

tinguished from the red absorption-line and bluer emission-line galaxies. The poststarburst galaxies are blue, although not as blue as the the galaxies with strong emission lines.

Some of our poststarburst galaxies display very strong Balmer lines (<Hδ+Hγ+Hβ> $\gtrsim$ 8 Å), indicating recent, massive bursts of star formation. Models have indicated that star bursts comprising upwards of 20% of the mass of the galaxy are required to achieve such large Balmer line strengths (Dressler & Gunn 1983, Poggianti & Barbaro 1996). The lack of detectable emission features in these objects indicates that the star burst was highly efficient in converting gas to stars. The dominant A type spectrum also implies that the burst occurred approximately 1 Gyr before the epoch of observation. An example of such a flamboyant poststarburst object (with <Balmers>=9.1 Å) is shown in Figure 3.

The emission-line galaxy population contains those galaxies which, at the epoch of observation, are experiencing star formation at various levels. The cutoff for inclusion into the emission line category is the presence of [OII] 3727 Å emission with EW > 5 Å, with emission line detections at a level of >1 σ. The variety of emission-line galaxy behaviors is shown in Fig. 4, and includes late-type galaxies undergoing strong ([OII] 3727 Å EW > 50 Å) star formation at the epoch of observation (number 519), galaxies with emission lines *plus* strong Balmer absorption features (number 595), and red absorption-line galaxies with weak [OII] emission (number 369). The upper panel of Fig. 6 plots the distribution of [OII] emission line strength versus galaxy color, demonstrating a clear blueing trend with larger [OII] emission strength.[2] A similar correlation between [OII] emission and galaxy color is also seen for present-day spirals (Dressler & Gunn 1982).

There are 16 emission line galaxies with [OII] emission and Hδ absorption stronger than 4 Å; these are labeled "emi+Hδ" in Table 1. The last class of emission-line objects, red galaxies with weak emission ([OII] < 20 Å), includes galaxies 137, 143, 305, 369, and the brightest cluster galaxy 375. These galaxies have spectra dominated by absorption features yet also display weak emission. We infer that the star formation histories of these galaxies are, for the most part, similar to those of the rest of the absorption-line population except that they contain enough residual gas to allow a low rate of continued star formation. Nonetheless, because of the existence of emission lines in their spectra these objects are classified as "emi" in Table 1. Weak emission in nearby red brightest cluster, elliptical, and S0 galaxies is also often observed (e.g., Fisher, Franx, & Illingworth 1995; 1996).

The FMB study of CL 1358+62 classified 6 spectra as poststarburst. Here, our stricter poststarburst definition applies to only 2 of these spectra. The 4 remaining galaxies do show enhanced enhanced Balmer absorption compared with the average for the absorption line population. These galaxies display average Hδ line strengths of $\sim$4 Å compared to the 0.9 Å average for the 177 absorption line galaxies, and are probably weaker examples of the poststarburst phenomena. The galaxies meeting our strict definition of poststarburst have average Hδ absorption line strengths of

[2]A number of galaxies in the upper panel of Fig. 6 appear to have [OII] emission strengths above our emission-line galaxy cutoff (5 Å) yet are shown as absorption-line galaxies (*crosses*). The [OII] detections for these objects (mainly MMT spectra) are not significant at the 1σ level.

6.3 Å. All five of the galaxies classified by FMB as emission-line meet the emission-line galaxy criteria outlined above.

5.2. Comparison with Low-z Galaxy Spectra

In order to make possible connections between our cluster galaxy spectra and those from known morphological types and evolutionary sequences we have compared our CL 1358+62 spectra with spectra of present-day ($z \approx 0$) galaxies from the collections of Kennicutt (1992) and Liu & Kennicutt (1995). These are compilations of the integrated spectra of normal, peculiar, and merging galaxies enabling a valid comparison with spectra of distant galaxies such as we observe in CL 1358+62. We measured the EW of Hδ, Hγ, Hβ and [OII] 3727 Å for the 55 spectra in Kennicutt's atlas. The Liu & Kennicutt work tabulates these equivalent widths for their sample of merging galaxies.

To compare the star formation characteristics of the (non-merging) galaxies in Kennicutt's and the CL 1358+62 galaxies we plot the Hδ EW versus [OII] 3727 Å emission for both samples in the upper panel of Fig. 7. In both cases only measurements with errors for Hδ EW <5 Å are used. The points for the CL 1358+62 spectra are coded according to the spectral type definitions outlined in §5.1. One striking feature of the diagram is the absence of poststarburst galaxies in the Kennicutt atlas satisfying our criteria; all of Kennicutt's galaxies with strong Hδ absorption also show [OII] emission. In fact, the Kennicutt atlas contains just four galaxies with large Hδ absorption (> 5 Å) irrespective of [OII] emission strength. In contrast, our collection of CL 1358+62 spectra includes a variety of absorption-line, poststarburst, and emission-line galaxies with Hδ absorption EW > 5 Å.

Excluding the region occupied by the poststarburst galaxies, the absorption-line and emission-line galaxy sequences in CL 1358+62 span a locus similar to that of the nearby galaxies. This is interesting because the Kennicutt atlas contains a wide range of normal and peculiar Hubble types from the field and cluster environments: early-type elliptical and S0 galaxies, spirals, irregulars, starburst and active galaxies, and HII regions. This suggests that the galaxy population in CL 1358+62 also includes a wide variety of spectral and morphological types, although the mix is different in Kennicutts's sample and CL 1358+62.

The lower panel of Fig. 7 is similar to the upper panel, except the cluster galaxies are compared with the merging galaxy sample of Liu & Kennicutt (*solid squares*). This comparison is interesting because galaxy interactions have been offered as a possible mechanism leading to the formation of poststarburst galaxies (Lavery et al. 1992; Dressler et al. 1994; Couch et al. 1994). In particular, Zabludoff et al. (1996) selected a sample of 21 E+A galaxies from the Las Campanas Redshift Survey (LCRS; Shectman et al. 1996) and found that at least five displayed clear tidal features, suggesting that galaxy interactions or mergers could have played a role in their creation.

However, the lower panel of Fig. 7 shows that poststarburst galaxies meeting our criteria are absent from the Liu & Kennicutt catalog. Those galaxies with high Hδ absorption (>4 Å) EW also display at least moderate [OII] emission (5 Å$<$ [OII] EW <15 Å). Liu & Kennicutt suggest that a number of galaxies in their sample with Hδ EW >6 Å and [OII] EW <15 Å have spectra similar to the

poststarburst (E+A) galaxies in distant clusters. However, these merging galaxy spectra more closely resemble the emi+Hδ spectral type (§5.1) due to the choice of an [OII] EW cutoff of 15 Å . These Hδ-strong galaxies with emission have been observed in other intermediate redshift clusters (e.g. Abraham et al. 1996) and may be in an evolutionary phase distinct from that of the E+A galaxies.

6. Cluster Structure as a Function of Spectral Type

It has been frequently noted that early-type galaxies predominate in dense cluster environments (Hubble & Humason 1931; Morgan 1961; Abell 1965; Oemler 1974), and one of our prime objectives in studying CL 1358+62 is to search for evolution in the morphology-density or morphology-radius relation. The van Dokkum et al. (1997) study gives morphological classifications for 194 galaxies in our sample that lie within the boundaries of the mosaic of available HST images. A future paper will investigate in depth the relationship between these galaxy morphologies and the spectral types presented here. Here, we note only that there is a clear connection between the spectral types that we define and the galaxy morphologies. Our galaxies with absorption-line spectra typically display elliptical and S0 galaxy morphologies while the galaxies with strong emission lines correspond to late-type spiral and irregular galaxies.

6.1. Spectral Type as a Function of Local Galaxy Density

Here, we study the distribution of the different spectral types as a function of local galaxy surface density and compare this with Dressler's galaxy morphology-density relation. We calculate surface number densities according to the Dressler (1980) prescription: for each cluster galaxy the ten nearest cluster galaxies are found and the distance to the tenth object is used to compute the area enclosing all 11 objects (πr_{10}^2). A local density, $\rho_{\rm proj}$=$11/\pi r_{10}^2$, can then be assigned to each galaxy. The resulting relation between spectral type and galaxy surface density for CL 1358+62 is shown in the upper panel of Figure 8. There are 46 or 47 galaxies in each of the bins in Fig. 8.

From Fig. 8 it is clear that the distributions of spectral types do vary as a function of local galaxy density. A Kolmogorov-Smirnov (KS) test indicates that the distribution of absorption-line and emission-line galaxies with galaxy density were not drawn from the same parent population with 99.84% confidence. In our highest density bin (>71 galaxies Mpc^{-2} with average $\rho_{\rm proj}$=168 galaxies Mpc^{-2}) 87±14% have pure absorption line spectra, 9±4% have emission line spectra and 4±3% have poststarburst spectra. In the highest density regions studied by Dressler (1980) in rich clusters at low redshift ($\rho_{\rm proj}$=100 gals Mpc^{-2}) he found 88% S0+E galaxies and 12% S+Irr galaxies.

In the lowest density regions of CL 1358+62 ($\rho_{\rm proj}$<13 gals Mpc^{-2} with average $\rho_{\rm proj}$=8 gals Mpc^{-2}) 54±15% have pure absorption line spectra and 46±14% have emission line spectra. This census may be compared with a similar low density region (average $\rho_{\rm proj}$=1.3 gals Mpc^{-2}) from Dressler's cluster sample which contained 43% E+S0 galaxies and 57% S+Irr galaxies. These comparisons suggest that the spectral type-density relation in CL 1358+62 resembles in broad outline the morphology-density relation in Dressler's clusters at z∼0.04.

The fraction of poststarburst galaxies may

peak at intermediate galaxy surface density ($\rho_{\rm proj}\approx$35 gal Mpc^{-2}). No poststarburst galaxies are found in our lowest density bin. However, there are only 11 poststarburst galaxies in our sample so firm conclusions regarding their distribution await additional studies of intermediate redshift clusters.

6.2. Spectral Type as a Function of Clustercentric Radius

The lower panel of Figure 8 is a plot of the relative number fractions of the spectral types versus projected radius from the BCG. The absorption-line galaxies, the dominant population, define the cluster structure and show a smooth decrease in number fraction with increasing clustercentric radius. The fraction of emission-line galaxies increases steadily with clustercentric radius. The upper and lower panels of Figure 8 are qualitatively similar. A KS test indicates that at the 99.94% confidence level, the distribution of absorption-line and emission-line galaxies shown in the lower panel of Figure 8 are not drawn from the same parent population. At 97.52% confidence the absorption-line and Hδ+emission line galaxies are not drawn from the same parent population.

Within a projected radius of $r_{\rm p}$<0.4 Mpc 86±17% of the galaxies have absorption line spectra, 8±6% have poststarburst spectra, and 8±6% have emission-line spectra. This mix is consistent with the galaxy populations found in other cluster cores at intermediate redshift (e.g., Abraham et al. 1996). In the outermost radial bin (at $r_{\rm p}$=1.7 Mpc) 59±11% of the galaxies have pure absorption-line spectra and 41±9% have emission-line spectra. Of the latter group, 70% display vigorous star formation ([OII] EW $>$ 20 Å). There are no poststarburst galaxies in the outermost radial bin.

6.3. Projected Distribution as a Function of Spectral Type

The distributions of the various spectral types on the plane of the sky are shown in Figure 9. For the emi+Hδ, emission-line and poststarburst galaxies, the point size indicates the strength of Hδ absorption, [OII] emission, and Balmer line absorption, respectively. The absorption-line galaxies, as the dominant population, define the cluster structure while the poststarburst and emission-line galaxies are less clustered. A two-dimensional KS test indicates that the spatial distribution of the spectroscopically active galaxies could not have been drawn from the same parent sample as the absorption-line galaxies with 99.28% confidence.

The spatial distribution of emission-line galaxies appears to be nonuniform: 31 emission-line galaxies lie southwest of a line drawn through the origin from SE to NW, while 12 emission-line galaxies lie to the northeast of the line. We note that similar nonuniformities in emission-line galaxy spatial distributions have been seen in other intermediate redshift clusters (e.g., Abraham et al. 1996) and were used to argue for a preferred directions of subclustering or infall. However, simulations indicate that the emission-line galaxy distribution in CL 1358+62 is inconsistent with a symmetric distribution at only 82% confidence.

The poststarburst galaxy distribution in Fig. 9 appears to be aligned linearly along a roughly North-South direction. We note that the substructuring we find in CL 1358+62 and that found by the CNOC group (see §7) are also located along a N-S axis. However, we find that the apparent departure from a sym-

metric distribution is not statistically significant using a two-dimensional KS test.

6.4. Velocity Distributions of the Spectral Types

We use the prescriptions of Danese, De Zotti, & di Tullio (1980) to calculate the means and dispersions for the entire sample and for the different galaxy spectral types. We find a mean cz=98425±90 km s^{-1} (z= 0.32831±0.00030) and a velocity dispersion of 1027^{+51}_{-45} km s^{-1} for the entire sample of 232 galaxies. Figure 10 presents the velocity histograms for the absorption-line, poststarburst, emission-line, and emi+Hδ galaxies. It appears that the absorption-line galaxies have a lower dispersion than the poststarburst and emission-line galaxies.

The mean velocities and dispersions for each of the spectral types are summarized in Table 3. We also give the kinematic parameters for the 23 emission-line galaxies with weak [OII] emission (5 Å <[OII] EW<20 Å) and for the 21 with strong [OII] emission([OII] EW> 20 Å. None of the subgroupings of emission-line galaxies (the full sample of 44 emission-line galaxies, weak emission-line, strong emission-line, and the emi+Hδ) have mean velocities which differ by more than 1 σ from the mean velocity of the dominant absorption-line population.

The mean cz of the poststarburst galaxies differs from that of the absorption line galaxies by 1 σ and the dispersion differs by ∼2 σ. A KS test indicates that at 90% confidence the two velocity distributions are not drawn from the same parent population. We note that the velocity dispersion of freely infalling galaxies is expected to be $2^{1/2}$ times that of the virialized cluster core population. The ratio of the velocity dispersions of the spirals and ellipticals in both the Virgo (Huchra 1985) and Coma (Colless & Dunn 1996) clusters are of this order. Although the statistics are weak at present, the ratio of the velocity dispersions of the poststarburst and absorption-line galaxies in CL 1358+62 are also $\sim 2^{1/2}$.

The evidence for dynamical differences as a function of spectral type is strongest when we combine the poststarburst and emission line galaxies in a single "active" population. For galaxies with velocities within ±0.6 $\sigma_{\rm cl}$ of the cluster mean the active fraction is 16±4%, rising to 32±7% in the tails of the velocity distribution (∼2.0 $\sigma_{\rm cl}$ from the mean).

7. Subclustering

The many successful searches for velocity substructure in well-sampled galaxy clusters suggest that clusters continue to accrete galaxies to the present day (e.g., Geller & Beers 1982; Dressler & Shectman 1988; Fitchett & Webster 1987; Zabludoff, Franx, & Geller 1993; Colless & Dunn 1996). The manifestations of cluster substructure are varied and a multitude of tests have been devised to measure various types of substructures. These include counting nearest neighbors that satisfy velocity and dispersion criteria (Dressler & Schectman 1988), the KS two-sample test (Colless & Dunn 1996), searching for asymmetries in the shape of the velocity distribution (Zabludoff, Franx, & Geller 1993), and mixture-modeling algorithms (McLachlan & Basford 1988). No single technique is superior in all situations; their sensitivities to particular aspects of the observed velocity distribution vary. The various techniques differently weight the tails of the velocity distribution, regions of high or low galaxy density, or structures resolved in velocity space, but

superposed spatially, such as cluster cores.

We too have used a variety of methods to search for subclustering within CL 1358+62. Figure 11 plots redshift against projected radius. The cluster mean velocity as well as the redshift boundaries used to define cluster membership are shown (see §4). We see an excess of galaxies with redshifts lower than the cluster mean within a radius of 40″ (0.23 Mpc).

Following the technique outlined by Zabludoff, Franx, & Geller (1993) we have decomposed the full cluster velocity distribution into a sum of orthogonal Gauss-Hermite functions to quantify the asymmetric third-order (h_3) and symmetric fourth-order (h_4) terms of the distribution. This technique indicates that the velocity distribution of CL 1358+62 departs from a Gaussian with both asymmetric and symmetric distortions. We measure an h_3 of -0.088 ± 0.045 for the velocity distribution of all 232 cluster members. This result is significant at the 94.6% level. This asymmetric deviation is in the sense that CL 1358+62 has a tail of galaxies at redshifts lower than the cluster mean. The h_4 term for the velocity distribution of CL 1358+62 is -0.087 ± 0.042, which indicates that symmetric deviations are also present in the sense that the velocity distribution is broader than a Gaussian. This h_4 term is significant at the 97.8% confidence level.

We have calculated the Dressler & Shectman (1988) substructure statistic δ for each cluster member in CL 1358+62. The δ parameter is a measure of the deviation of any one galaxy from the local velocity mean and dispersion. In Figure 12 we plot δ as a function of projected position within the cluster. The results indicate that significant kinematic irregularities are present along the cluster center line-of-sight and towards the northwest corner.

The significance of these deviations has been calibrated with Monte Carlo simulations. A total of 1000 realizations were calculated in which the velocities of the 232 cluster members were randomly reassigned while fixing the galaxy positions. The cumulative deviation Δ, the sum of the δ's for the individual cluster members, is 315.6. According to our simulations, this cumulative deviation is significant at the 96% confidence limit. If the velocity distribution of CL 1358+62 were close to Gaussian and the local variations were random, then Δ would be of the same order as the total number of cluster members.

In Figure 13 we plot the Dressler-Shectman statistic as a function of velocity and each of two projected coordinates (x and y). We see that the dominant kinematic substructure is a group of 20 galaxies with velocities $95000<cz<97000$ projected close to the cluster center (projected radius $r_{\rm p}<95''$ centered at $x=-27''$ $y=-8''$). This is the same foreground group mentioned in connection with Fig. 11 that produces the low velocity tail found by the Gauss-Hermite analysis. The mean velocity of this group is 96272 ± 119 km s^{-1} with $\sigma=391^{+84}_{-53}$. We find a second subclump composed of 10 galaxies with velocities $99000<cz<101000$, centered at $x=77''$ $y=114''$with $r_{\rm p}<60''$. The mean velocity of this group is 99771 ± 136 km s^{-1} and $\sigma=314^{+112}_{-56}$.

Figure 14 plots contours of galaxy surface density in radial velocity intervals of 2000 km s^{-1}. The foreground subclump discussed above appears in the first velocity bin as a dense concentration of galaxies towards the cluster center. The middle velocity bin includes the bulk of the cluster members that

are roughly spherically distributed around the BCG at x=0 y=0. The background velocity bin shows a relatively empty cluster core as well as two areas of higher concentration to the north (the second subclump identified above) and south of the cluster center.

The foreground subclump (at a projected radius of 0.2 Mpc in a region with an average surface density of 125 galaxies Mpc^{-2}) consists of 80% absorption-line, 15% poststarburst, and 5% emission-line galaxies. This mix does not deviate significantly from the the cluster average at this projected radius and surface density. All 10 of the galaxies in the background subclump north of the cluster center have pure absorption-line spectra. This subclump has a projected radius of 0.8 Mpc and an average galaxy surface density of 46 galaxies Mpc^{-2}. At this projected radius and surface density the cluster as a whole contains ∼80% absorption line galaxies. Therefore, the subclumps do not appear to contain a peculiar mix of spectral types. Furthermore, the spectroscopically active galaxies do not have an excess or deficit of nearby companions.

The redshift distribution of CL 1358+62 has been studied previously by the CNOC group (Carlberg et al. 1996; Carlberg, Yee, & Ellingson 1997) who have amassed a catalog of 164 cluster galaxy redshifts. The redshift boundaries used for determining cluster membership are very similar for both studies. The CNOC field limits are 2′ narrower in R.A. than ours and extend to the same Declination to the north. However, the CNOC field extends 4′ further to the south and here the CNOC group detects a concentration of galaxies with cz differing by 1000 km s^{-1} from the cluster center's cz. This feature leads the CNOC group to classify CL 1358+62 as a binary cluster.

8. Summary and Conclusions

Our investigation of CL 1358+62 is based on a catalog of 232 cluster galaxy spectra. We combine the velocity, spatial, and spectral information from our catalog to study the cluster structure. Similar to other rich clusters, the dominant galaxy population in CL 1358+62 is composed of red, absorption-line galaxies with passively evolving stellar populations that formed the majority of their stars long ($>$ 5 Gyr) before the epoch of observation. The absorption-line galaxies make up 76% of the total cluster population, rising to ∼90% of the galaxies with velocities within 0.6 $\sigma_{\rm cl}$ of the cluster mean and located within the central $r_{\rm p}$<0.4 Mpc.

Our sample concentrates on the central main body of the cluster ($r_{\rm p}$<2 Mpc). We note that the CNOC project had previously found evidence for a second concentration south of the cluster center, just outside our field limits (Carlberg et al. 1996, Carlberg, Yee, & Ellingson 1997). Significant evidence for substructure in the central part of the cluster is seen. We find that the distribution of line-of-sight velocities for CL 1358+62 departs significantly from a Gaussian. Two compact (with projected radii $r_{\rm p}$<90″ and $\sigma\leq$400 km s^{-1}) subclumps are found in the cluster, one with a mean z higher than that of the cluster as a whole, and one with a lower mean z. This subclustering implies that CL 1358+62 has not yet reached equilibrium and is still in the process of virialization and accretion of new members. The galaxies in these subgroups have primarily absorption-line spectra, indicating that accretion into groups may play an important role in the spectral evolution of galaxies.

The relations between spectral type and radius/galaxy density in CL 1358+62 are qualitatively similar to the morphology-radius or morphology-density relations seen in nearby clusters (i.e., Dressler 1980; Whitmore, Gilmore, & Jones 1993). That the galaxy mix in CL 1358+62 has reached proportions similar in magnitude and distribution to those seen in nearby rich clusters is indicative of its advanced state of evolution. Similar results have been seen in the cores of other intermediate redshift clusters (Couch et al. 1997; Dressler et al. 1997) which are dynamically evolved and centrally concentrated.

The gradients in the spectral mix as a function of radius and local density indicate that the mean ages of the galaxy stellar populations decrease with increasing distance from the cluster center. This is evidenced by the increase in emission-line galaxy fraction with increasing clustercentric radius. These results are consistent with the idea that the galaxy evolution in CL 1358+62 is shaped by the accretion of infalling field galaxies whose star formation rates are diminished upon cluster entry. Similar conclusions were reached by Abraham et al. (1996) in their study of the intermediate redshift (z=0.228) cluster Abell 2390.

Spectrally active galaxies make up 23±3% of the cluster population; 4/5 of these have emission-line spectra indicating continuing star formation while the remainder have poststarburst ("E+A") spectra. This fraction of spectrally active galaxies is consistent with the elevated proportion (compared to low-z) observed for samples of distant clusters at similar redshifts (Dressler & Gunn 1983; Couch & Sharples 1987; Abraham et al. 1996). For CL 1358+62, the fraction of spectroscopically active galaxies increases in the tails of the velocity distribution, lending further support to the hypothesis that galaxies with current or recent signs of star formation have recently been accreted. However, the high relative velocities could also be explained if the spectrally active galaxies were preferentially located in radial orbits.

Poststarburst galaxies make up 5% of the CL 1358+62 cluster population. This can be compared to the Las Campanas Redshift Survey (LCRS), which contained just 0.2% "E+A" galaxies (Zabludoff et al. 1996). This sample is typical of the nearby field ($0.05<z<0.13$). However, the definition Zabludoff et al. applied to select poststarburst galaxies was stricter than the one used here. If our definition is used, 1% of the LCRS sample are poststarburst galaxies (Zabludoff, private communication). The origin of these field poststarburst galaxies is still an open question although galaxy-galaxy interactions have been offered as a possibility (Zabludoff et al. 1996).

We have addressed the question of whether the poststarburst galaxy spectra in CL 1358+62 resemble those found for major mergers by making a comparison between our "E+A" spectra and spectra of nearby merger remnants from Kennicutt (1992) and Liu & Kennicutt (1995). We find that none of the major merger spectra satisfy our poststarburst selection criteria. All of the nearby merger remnants have detectable [OII] 3727Å emission with equivalent widths larger than 5Å. This implies that the CL 1358+62 "E+A" galaxies are either not formed by major mergers, or that a process operates that removes the gas from the mergers very quickly after the merger event. Interactions with and/or stripping by the intracluster medium (Gunn & Gott 1972; Bothun & Dressler 1986) may be an effective mechanism for removing the

remaining gas in merging cluster galaxies. We note that galaxy-galaxy interactions that are less severe than the major mergers of Liu & Kennicutt have also been offered as a mechanism for truncating star formation in accreting galaxies (Moore et al. 1996).

If larger samples confirm our tentative observation that poststarburst galaxies are absent in the outermost, lowest density regions of clusters, we might conclude that an infalling galaxy must penetrate to regions where galaxy-galaxy interactions, stripping from the intracluster medium, or interaction with the cluster potential become strong enough to drive their evolution. The Hδ-strong galaxies with [OII] emission might then represent an intermediate state in a single evolutionary sequence from infalling spiral/irregular to poststarburst galaxy. If so, then the emi+Hδ galaxies must abruptly exhaust their gas supply and terminate star formation while the Balmer absorption line strengths are still large. We are currently comparing the morphologies of the emi+Hδ and poststarburst galaxies in CL 1358+62 (using the HST images, §2) in order to address this issue. We note that Barger et al. (1996) have constructed models that suggest similar evolutionary sequences.

The catalog that we present for CL 1358+62 at z=0.328 is the largest available for a cluster at z>0.1. In a companion study, van Dokkum et al. (1997) investigated the color-magnitude relation for CL 1358+62 using a wide field mosaic of multi-color HST WFPC2 images. This combination of a magnitude-limited spectroscopic survey and high resolution HST imaging has allowed us to study CL 1358+62, an object with a lookback time $\sim$1/3 the present age of the Universe, at a level of detail heretofore only attained for a tiny handful of nearby clusters. Our overall goal is to elucidate the key mechanisms governing galaxy evolution by obtaining HST mosaics and ground-based spectra for rich clusters at increasing redshift.

Although our program is initially focussed on cluster galaxies, we also serendipitously obtain spectra and images of the foreground and background galaxies along the cluster line-of-sight (e.g. Franx et al. 1997). We are therefore able to study the stellar populations of field objects with the same level of detail as our cluster galaxies. The spectral and WFPC2-derived morphological characteristics of these galaxies are currently being examined and results will be presented in forthcoming works.

MF thanks the Center for Astrophysics for its hospitality during several visits. We gratefully acknowledge support from a grant of the University of Groningen.

This research has made use of the NASA/IPAC Extragalactic Database (NED) which is operated by the Jet Propulsion Laboratory, Caltech, under contract with the National Aeronautics and Space Administration.

REFERENCES

Abell, G. O. 1965, ARA&A, 3, 1

Abraham, R. G., Smecker-Hane, T. A., Hutchings, J. B., Carlberg, R. G., Yee, H. K. C., Ellingson, E., Morris, S., Oke, J. B., & Rigler, M. 1996, ApJ, 471, 694

Allington-Smith, J., Breare, M., Ellis, R., Gellatly, D., Glazenbrook, K., Jorden, P., Maclean, J., Oates, P., Shaw, G., Tanvir, N., Taylor, K., Taylor, P., Webster, J., & Worswick, S. 1994, PASP, 106, 983

Barger, A. J., Aragon-Salamanca, A., Ellis, R. S., Couch, W. J., Smail, I., & Sharples,

R. M. 1996, MNRAS, 279, 1

Bothun, G. D., & Dressler, A. 1986, ApJ, 301, 57

Burstein, D., & Heiles, C. 1984, ApJS, 54, 33

Butcher, H. R., & Oemler, A., Jr. 1978, ApJ, 219, 18

Butcher, H. R., & Oemler, A., Jr. 1984, ApJ, 285, 426

Carlberg, R. G., et al. 1994, JRASC, 88, 39

Carlberg, R. G., Yee, H. K. C., Ellingson, E., Abraham, R., Gravel, P., Morris, S., & Pritchet, C. J. 1996, ApJ, 462, 32

Carlberg, R. G., Yee, H. K. C., & Ellingson, E. 1997, ApJ, 478, 462

Colless, M., & Dunn, A. M. 1996, ApJ, 458, 435

Couch, W. J., & Sharples, R. M. 1987, MNRAS, 229, 423

Couch, W. J., Ellis, R. S., Sharples, R. M., & Smail, I. 1994, ApJ, 430, 121

Couch, W. J., Barger, A. J., Smail, I., Ellis, R. S., & Sharples, R. M. ApJ, in press

Danese, L., De Zotti, G., & di Tullio, G. 1980, A&A, 82, 322

Dressler, A. 1980, ApJ, 236, 351

Dressler, A., & Gunn, J. E. 1982, ApJ, 263, 533

Dressler, A., & Gunn, J. E. 1983, ApJ, 270, 7

Dressler, A., & Shectman, S. A. 1988, AJ, 95, 985

Dressler, A., Oemler, A., Butcher, H. R., & Gunn, J. E. 1994, ApJ, 430, 107

Dressler, A., Oemler, A., Couch, W. J., Smail, I., Ellis, R. S., Barger, A., Butcher, H., Poggianti, B. M., & Sharples, R. M. 1997, ApJ, in press

Evrard, A. E. 1993, in The Environment and Evolution of Galaxies, ed. J. M. Shull & H. A. Thronson, Jr. (Dordrecht: Kluwer), 69

Fabricant, D. G., McClintock, J. E., & Bautz, M. W. 1991, ApJ, 381, 33 (FMB)

Fisher, D., Franx, M., & Illingworth, G. 1995, ApJ, 448, 119

Fisher, D., Franx, M., & Illingworth, G. 1996, ApJ, 459, 110

Fitchett, M. J., & Webster, R. L. 1987, ApJ, 317, 653

Franx, M., Illingworth, G., Kelson, D. D., van Dokkum, P. G., & Tran, K.-V. 1997, ApJ, 486, L75

Geller, M. J., & Beers, T. C. 1982, PASP, 94, 421

Gioia, I. M., Maccacaro, T., Schild, R. E., Wolter, A., Stocke, J. T., Morris, S. L., Henry, J. P. 1990, ApJS, 72, 567

Gioia, I. M., & Luppino, G. A. 1994, ApJS, 94, 583

Gunn, J. E., & Gott III, R. J. 1972, ApJ, 176, 1

Huchra, J. P. 1985, in ESO Workshop Proc. No. 20, The Virgo Cluster, ed. O. G. Richter & B. Binggeli (Munich:ESO), 181

Hubble, E., & Humason, M. L. 1931, ApJ, 74, 43

Jarvis, J., & Tyson, J. 1981, AJ, 86, 976

Jones, L. A., & Worthey, G. 1995, ApJ, 446, L31

Kennicutt, R. C. 1992, ApJS, 79, 255

Koo, D. 1988, in Towards Understanding Galaxies at Large Redshift, ed. R. Kron & A. Renzini (Dordrecht: Kluwer), 275

Kurtz, M. J., Mink, D. J., Wyatt, W. F., Fabricant, D. G., Torres, G., Kriss, G. A., Tonry, J. L. 1992, in Astronomical Data Analysis Software and Systems I, A.S.P. Conference Series Vol. 25, ed. D. M. Worrall, C. Biemesderfer, & J. Barnes, p. 432

Lauer, T. R., Stover, R. J., & Terndrup, D. 1983, The VISTA User's Guide (Lick Obs. Tech. Rep. 34) (Santa Cruz: Univ. California)

Lavery, R. J., Pierce, M. J., Mcclure, R. D. 1992, AJ, 104, 2067

Liu, C. T., & Kennicutt, R. C. 1995, ApJ, 450, 547

Luppino, G. A., Cooke, B. A., McHardy, I. M., Ricker, G. R., 1991, AJ, 102, 1

McLachlan, G. J., & Basford, K. E. 1988, Mixture Models: Inference and Applications to Clustering (New York: Marcel Dekker)

Moore, B., Katz, N., Lake, G., Dressler, A., & Oemler, A. 1996, Nature, 379, 613

Morgan, W. W. 1961, Proc. Natl. Acad. Sci., 47, 905

Oemler, A. 1974, ApJ, 194, 1

Poggianti, B. M., & Barbaro, G. 1996, A&A, 314, 379

Shectman, S. A., Landy, S. D., Oemler, A. A., Tucker, D. L., Lin, H., Kirshner, R. P., & Schechter, P. L. 1996, ApJ, 470, 172

Tonry, J., & Davis, M. 1979, AJ, 84, 1511

Valdes, F. 1982a, Faint Object Classification and Analysis System, Central Computer Services, NOAO

Valdes, F. 1982b, SPIE Proc., 331, 465

van Dokkum, P. G., Franx, M., Illingworth, G. D., Kelson, D. D., Fisher, D., & Fabricant, D. 1997, ApJ, in press

Whitmore, B. C., Gilmore, D. M., & Jones, C. 1993, ApJ, 407, 489

Yee, H. K. C., Ellingson, E., & Carlberg, R. G. 1996, ApJS, 102, 269

Zabludoff, A. I., Franx, M., & Geller, M. J. 1993, ApJ, 419, 47

Zabludoff, A. I., Zaritsky, D., Lin, H., Tucker, D., Hashimoto, Y., Shectman, S. A., Oemler, A., & Kirshner, R. P. 1996, ApJ, 466, 104

This 2-column preprint was prepared with the AAS LaTeX macros v4.0.

Fig. 1.— Spatial distribution for all galaxies (*open circles*) in our photometric catalog with R magnitudes brighter than 21. Galaxies for which redshifts were measured are marked by *crosses*. The two regions enclosed by the *large dotted circles* indicate areas where bright stars prevented data from being collected. The rectangular region outlined by the dotted lines delineates the area where we have concentrated our spectroscopy.

Fig. 2.— Completeness of the redshift sample as a function of magnitude. Each point gives the ratio of the number of galaxies for which redshifts were measured to the total number of possible galaxies. The completeness is shown for each galaxy in running bins of ± 0.50 mag for galaxies brighter than R=20.0 mag, and bins of ± 0.25 mag for galaxies fainter than R=20.0 mag. The position of the brightest cluster galaxy is marked with an arrow.

Fig. 3.— Deredshifted spectrum of the poststarburst cluster galaxy 243 with the Balmer line strength indice definitions superimposed. The horizontal lines delineate the regions covered by the feature bandpasses and the pairs of vertical lines on each side of the indice show the regions covered by the associated continuum sidebands.

Fig. 4.— Examples of spectra for the various galaxy spectral types. The object identifier is given for each of the deredshifted galaxies. The top left panel displays the spectrum of a strong emission line galaxy (519) with very blue colors and a host of emission lines: [OII] 3727 Å, [NeIII] 3869 Å, Hδ, Hγ, [OIII] 4959 Å, Hβ, [OIII] 5007 Å, and Hα. The top right spectrum is for a late-type galaxy (595) in CL 1358+62 showing both emission and strong balmer absorption features. The lower left panel displays the spectrum of an absorption-line galaxy (369) with weak [OII] 3727 Å emission and the lower right panel shows the spectrum from one of the brighter absorption-line galaxies (353) in the cluster with no emission features.

Fig. 5.— Distribution of the average Balmer line strength, (Hδ+Hγ+Hβ)/3, for the full sample of cluster galaxies (*bold solid line*) and for those without measureable OII 3727 Å emission (*dotted line*). The distributions display a tail of galaxies with high Balmer line strengths (average>4.0 Å) which we use to identify the poststarburst population.

Fig. 6.— Balmer absorption and emission line strengths as a function of galaxy color. *Crosses* are used to represent the normal absorption-line dominated red galaxy population, *triangles* are shown for all the galaxies with the [OII] 3727 Å emission line in their spectra, and *circles* are used for the galaxies displaying poststarburst (no emission lines and strong Balmer absorption features) spectra. Note the clear separations of these different spectral types in these diagrams.

Fig. 7.— Hδ line strength plotted versus [OII] 3727 Å emission line strength. *Crosses* denote the absorption-line galaxies in CL 1358+62, *triangles* are shown for the emission-line galaxies, and *circles* represent the poststarburst galaxies. In the top panel *open squares* are used for measurements from Kennicutt's atlas of nearby galaxy spectra and the *filled squares* in the bottom panel shows results for nearby merging galaxies from Liu & Kennicutt.

Fig. 8.— Number fractions of the various

spectral types versus projected galaxy surface number density and clustercentric radius. *Crosses* are used to represent the normal absorption-line dominated galaxy population (**abs**), *triangles* are shown for all the galaxies with the [OII] 3727 Å emission line in their spectra (**emi**), and *circles* are used for the galaxies displaying poststarburst spectra (**E+A**). Note the absence of poststarburst galaxies in the low density, outermost radial regions.

Fig. 9.— Spatial distributions of galaxies in CL 1358+62 as a function of spectral type. *Crosses* are used to represent the normal absorption-line dominated galaxy population (**abs**), *squares* denote emission line galaxies which also display strong (>4 Å) Hδ absorption (**emi+H**δ), *triangles* are shown for all the galaxies with emission lines in their spectra (**emi**), and *circles* are used for the galaxies displaying poststarburst (no emission lines and strong Balmer absorption features) spectra (**e+a**). The symbol sizes for the emi+Hδ, emi, and E+A galaxies are scaled linearly with the strength of the Hδ feature, [OII] 3727 Å emission line, and Balmer lines (<Hδ+Hγ+Hβ>), respectively.

Fig. 10.— Velocity distributions as a function of spectral type. The absorption-line galaxies (**abs**) display a velocity distribution which is not as broad as that shown by the emission line galaxies (**emi**) and the emission-line galaxies with Hδ absorption (**emi+H**δ). The poststarburst galaxies (**E+A**) are uniformly distributed in redshift throughout the cluster with large dispersion. The *solid dot* in each panel denotes the redshift of the brightest cluster galaxy. The downward pointing arrow shows the mean velocity for each distribution and the dispersion is also given.

Fig. 11.— Redshift-projected radius distribution for the various spectral types. *Crosses* are used to represent the absorption-line galaxy population and *circles* are used for the galaxies displaying poststarburst spectra. Strong emission line galaxies ([OII] 3727 Å>20) are displayed as *large triangles* and weak emission line galaxies are given *small triangles*. The central dotted line is located at the mean redshift of the cluster and the upper and lower dotted lines denote the 4 $\sigma_{\rm cl}$ boundaries used for the definition of cluster membership. The brightest cluster galaxy is placed on the figure as the innermost r_p point (note that the BCG displays weak emission).

Fig. 12.— Positional map of the Dressler-Shectman statistic for all galaxies in our catalog of CL 1358+62. The position of each galaxy is marked by a circle whose diameter scales linearly with the deviation of the local kinematics, as determined from the galaxy and its ten nearest neighbors, from the global kinematics. The concentrations of large circles in the regions of the cluster center and towards the upper-right quadrant indicate correlated spatial and kinematic variations.

Fig. 13.— Position-velocity diagrams of the Dressler-Shectman statistic for CL 1358+62. The narrow distribution of galaxies found near the cluster center (x and $y < 100''$) and stretching from cz=95000 to ∼97000 km s^{-1} constitutes a foreground group. At redshifts beyond 99000 km s^{-1} a concentration of galaxies is found at y≈100″ and x≈50″.

Fig. 14.— Redshift channels showing the distribution of cluster members in both spatial and velocity dimensions. The channels are centered on the indicated redshifts and spaced

at intervals of 2000 km s^{-1}. Absorption-line galaxies are plotted as *crosses*, poststarburst galaxies are shown as *squares*, and emission-line galaxies are shown as *triangles*. Contours of galaxy surface number density are shown. All panels have the same contour settings. The cluster can be roughly divided into three main segments: a foreground group at $95000<cz<97000$ km s^{-1}, the main cluster component at $97000<cz<99000$ km s^{-1}, and an empty core with a background group at $99000<cz<101000$ km s^{-1}.

TABLE 1
CL 1358+62 CATALOG

Num	x(″)	y(″)	R	$V-R$	z	$\varepsilon(z)$	Hδ	Hγ	Hβ	[OII]	Notes
5	−148.78	−339.68	20.28	···	0.32720	0.00020	−0.6±2.3	−0.2±4.0	1.2±1.8	1.1±3.5	abs
7	−78.99	−337.52	20.71	···	0.33204	0.00020	1.9±4.2	0.1±3.9	−0.1±3.1	−17.3±4.8	emi
14	30.86	−332.21	19.96	···	0.32636	0.00020	3.7±2.1	3.1±2.8	−0.1±1.9	−7.1±2.2	emi
28	236.73	−313.15	21.36	···	0.32987	0.00020	6.2±7.6	−0.3±7.2	0.7±4.2	−25.7±9.7	emi
43	−24.43	−302.29	20.10	···	0.32486	0.00020	−0.7± 2.1	−3.3±1.0	2.3±1.2	−0.3±2.3	abs
49	−37.09	−289.42	20.58	···	0.32609	0.00020	1.2± 4.6	1.2±6.1	3.5±2.5	1.4±4.0	abs
53	268.95	−283.77	20.42	···	0.32989	0.00020	−2.3± 1.6	−0.5±3.0	1.5±1.6	1.1±3.1	abs
55	187.82	−282.34	20.66	···	0.33289	0.00038	6.4±3.2	0.6±4.0	−0.9±2.1	−16.1±5.0	emi+Hδ
57	254.48	−281.28	20.66	···	0.32684	0.00020	−6.9± 7.2	0.1±5.7	2.3±2.4	0.4±18.4	abs
77	−142.29	−268.16	21.56	···	0.32993	0.00034	4.1± 4.9	1.0±3.7	−0.2±4.3	−0.2±4.2	abs
78	221.26	−259.74	21.07	···	0.33154	0.00020	1.2±3.5	3.0±5.3	5.6±1.5	5.4±7.0	abs
86	−60.93	−252.59	21.72	···	0.33105	0.00023	1.0± 3.1	2.5±2.2	3.0±2.1	−6.4±7.0	abs
89	−73.05	−245.80	20.06	···	0.32631	0.00020	−1.3± 1.8	0.7±2.0	2.6±1.4	−0.8±2.5	abs
92	137.23	−237.13	20.80	···	0.32590	0.00025	5.7±3.0	2.6±3.2	2.3±2.6	0.0±2.5	abs
95	63.53	−235.36	20.48	0.89	0.31958	0.00020	1.1±3.4	5.7±3.2	2.0±2.2	0.6±4.4	abs
97	−64.22	−233.80	20.75	0.73	0.32437	0.00023	1.5±5.4	2.2±4.0	0.4±2.2	−12.9±3.6	emi
100	81.23	−230.40	19.79	0.85	0.33256	0.00020	0.9±2.0	1.5±3.0	3.5±1.6	0.2±3.1	abs
105	130.37	−222.09	21.46	0.65	0.32831	0.00020	0.8±4.7	1.3±2.4	3.1±1.5	−5.8±6.9	abs
108	−131.10	−224.99	20.65	0.92	0.32844	0.00020	−0.7±2.2	0.4±2.8	2.8±1.3	1.7±2.6	abs
109	73.68	−222.07	21.43	0.67	0.32270	0.00020	8.1±2.8	7.5±2.9	5.3±2.0	−0.1±4.3	e+a
110	58.61	−221.72	20.09	0.91	0.33291	0.00020	−0.5±2.0	0.9±1.8	3.0±1.5	−0.6±3.5	abs
126	67.93	−208.17	20.18	0.90	0.32259	0.00020	−1.0±1.3	0.3±2.4	2.8±1.6	2.1±1.8	abs
129	127.68	−201.66	20.10	0.82	0.32801	0.00020	0.0±1.7	1.0±1.4	2.6±0.7	−3.9±1.5	abs
132	87.39	−200.89	22.17	0.61	0.32658	0.00020	6.5±3.9	6.8±4.9	−2.3±3.0	−12.8±5.5	emi+Hδ
135	−21.15	−199.51	20.73	0.86	0.32590	0.00020	−0.6±3.1	1.4±3.5	4.0±2.8	−4.3±4.9	abs
137	86.00	−196.95	21.58	0.76	0.31922	0.00029	8.0±5.5	0.1±9.9	4.1±3.2	−12.8±7.6	emi+Hδ
142	−50.94	−191.34	20.35	0.95	0.32603	0.00020	0.8±4.4	−0.2±3.2	2.6±1.6	1.0±2.8	abs
143	57.97	−189.63	21.05	0.87	0.33305	0.00020	0.7±3.1	4.3±4.5	3.3±2.9	−8.5±5.9	emi
145	213.24	−187.43	21.08	···	0.33088	0.00034	−3.3± 4.0	−8.9±6.3	−13.2± 4.0	−53.9±5.6	emi
149	−147.60	−187.00	20.97	0.96	0.33020	0.00020	−1.2±3.7	0.4±4.5	2.1±1.5	4.0±3.1	abs
158	222.69	−173.34	20.07	···	0.32822	0.00020	−0.9± 1.3	−0.5±1.7	3.1±1.1	0.3±1.9	abs
164	−105.06	−172.23	19.95	0.95	0.32248	0.00020	−1.4±3.7	0.2±2.9	2.3±1.4	0.9±3.0	abs
167	89.31	−168.19	21.53	0.65	0.33447	0.00023	9.7±4.4	10.2±3.8	3.0±3.5	−3.6±6.1	e+a
171	93.66	−164.35	21.74	0.65	0.32822	0.00020	2.6±4.3	5.4±3.9	−1.4±2.7	−7.8±4.4	emi
178	−1.61	−155.08	20.57	0.51	0.32531	0.00020	5.4±3.6	4.3±2.2	−9.0±3.5	−34.2±1.7	emi+Hδ
182	−177.65	−152.25	21.07	0.91	0.33120	0.00023	−1.3±3.8	2.1±4.2	1.9±2.4	−0.7±3.5	abs
187	263.32	−141.80	21.75	···	0.33172	0.00028	3.5±4.4	0.3±6.5	2.8±6.0	5.3±9.1	abs
190	61.33	−142.74	21.80	0.69	0.33442	0.00031	6.9±2.4	1.7±5.2	3.0±2.7	−3.6±3.8	abs
192	13.83	−142.88	21.27	0.63	0.32804	0.00020	2.9±3.6	1.5±6.8	−3.8±6.2	−34.0±3.5	emi
200	−12.63	−138.44	20.04	0.81	0.33680	0.00040	4.8±4.0	−0.3±6.8	5.6±2.8	−4.0±5.9	abs
203	25.25	−137.36	20.86	0.91	0.32495	0.00020	1.5±4.6	3.8±3.7	3.6±2.7	2.2±4.0	abs
204	269.67	−132.66	19.74	···	0.33274	0.00020	−0.1± 2.3	−1.2±2.9	1.9±1.4	3.7±2.0	abs
205	−106.81	−135.88	21.76	0.89	0.32544	0.00020	5.5±6.1	2.0±5.7	1.7±2.2	7.3±5.1	abs
206	−165.28	−135.64	21.48	0.82	0.33321	0.00027	7.2±2.0	1.6±4.9	2.5±2.1	−7.5±7.6	abs
207	73.35	−130.84	21.86	0.78	0.33450	0.00020	0.9±3.6	−0.8±7.5	2.7±2.1	−0.1±6.1	abs
209	29.25	−130.76	19.97	0.72	0.33133	0.00020	5.9±1.1	6.9±1.6	5.2±1.3	−0.8±2.8	e+a
210	−185.02	−132.14	20.39	1.02	0.32251	0.00020	−2.7±2.9	1.3±2.1	2.6±1.6	3.2±4.2	abs
211	26.11	−129.35	20.10	0.91	0.32850	0.00020	0.7±1.3	2.2±3.0	2.4±0.7	0.7±1.4	abs
212	135.61	−127.67	20.16	0.93	0.32724	0.00020	−2.2±3.5	−0.8±3.9	2.7±1.5	−2.9±6.5	abs
215	28.54	−127.40	20.71	1.01	0.32565	0.00020	−0.3±4.5	2.7±3.6	1.9±2.5	0.7±3.7	abs
226	−208.35	−120.30	21.26	0.70	0.33222	0.00020	4.8±2.7	2.9±4.0	3.3±1.8	0.8±3.5	abs
227	15.91	−117.08	21.00	0.96	0.33194	0.00022	1.2±2.7	2.9±4.8	2.4±1.4	0.5±5.6	abs
233	−164.92	−114.30	19.49	0.97	0.33015	0.00020	−0.9±1.6	0.4±1.4	3.3±0.9	1.4±1.9	abs
234	111.84	−110.76	20.13	0.73	0.32870	0.00020	1.9±1.8	1.3±3.0	−3.1±1.8	−14.3±2.4	emi
235	−46.46	−111.33	21.55	0.87	0.33102	0.00022	1.0±3.3	3.1±3.8	0.2±2.8	1.3±6.5	abs
236	−37.20	−110.38	20.22	0.99	0.33500	0.00027	1.0±1.8	0.1±5.7	3.1±2.0	4.6±3.2	abs
239	−26.80	−103.88	20.72	0.99	0.32917	0.00020	−1.0±3.2	1.2±3.0	3.3±2.2	3.7±4.1	abs

TABLE 1—*Continued*

Num	x(″)	y(″)	R	$V-R$	z	$\varepsilon(z)$	Hδ	Hγ	Hβ	[OII]	Notes
242	−8.55	−101.16	19.88	0.95	0.32570	0.00027	0.3±3.3	0.0±3.8	2.0±1.8	5.0±2.6	abs
243	−13.78	−99.71	21.29	0.62	0.32892	0.00020	10.4±1.3	10.9±1.7	6.0±1.7	2.1±3.4	e+a
244	273.59	−95.30	20.87	···	0.33248	0.00020	2.3±1.5	2.4±2.3	−0.2±1.5	−11.4±1.2	emi
246	78.11	−96.07	21.08	0.92	0.32718	0.00020	3.4± 4.0	3.5±3.4	3.1±2.2	3.4±8.4	abs
248	−59.75	−96.18	20.32	1.05	0.32919	0.00020	−1.6±2.5	−1.1±2.4	2.7±0.9	2.5±4.7	abs
254	−63.46	−91.22	20.01	0.97	0.32280	0.00027	−0.4±3.0	−1.6±3.1	3.1±1.5	1.9±3.6	abs
256	−51.62	−88.49	19.00	1.00	0.32412	0.00041	3.0± 1.1	0.1±2.1	2.5±1.3	0.8±2.7	abs
264	−3.13	−79.26	22.12	0.42	0.33401	0.00020	3.3± 2.5	−1.8±3.2	−14.3±3.4	−58.8±5.6	emi
265	58.95	−77.87	20.57	0.96	0.33310	0.00040	5.0± 3.0	1.3±4.6	1.0±1.8	0.7±1.6	abs
269	−16.73	−76.88	19.12	1.02	0.32920	0.00027	0.1± 1.6	0.4±2.9	2.6±1.4	0.7±1.7	abs
271	−138.19	−78.11	21.78	0.54	0.32451	0.00027	4.5± 3.3	−1.2±2.2	−13.0±4.1	−55.1±4.8	emi+Hδ
272	−53.03	−76.45	20.99	0.93	0.33010	0.00040	−3.6±4.3	1.8±4.3	0.5±1.3	−3.5±6.0	abs
278	−19.71	−73.64	20.57	0.99	0.33089	0.00044	0.1± 2.5	−1.4±2.3	2.4±0.7	2.3±3.4	abs
279	69.25	−72.37	20.57	0.97	0.32396	0.00055	1.6± 3.7	1.1±4.2	4.8±2.5	1.8±3.1	abs
283	−176.74	−72.38	20.54	0.92	0.33183	0.00020	−0.1±2.8	1.3±3.8	3.2±1.3	−0.3±3.8	abs
285	1.91	−68.62	21.58	1.01	0.33680	0.00040	−9.3±8.9	−2.7±7.8	−0.6±5.2	7.1±13.0	abs
288	−75.07	−68.20	20.69	0.99	0.31940	0.00027	−1.3±4.0	1.4±3.8	0.1±1.3	0.2±8.9	abs
290	15.96	−65.50	21.08	0.74	0.33610	0.00040	3.7± 1.1	1.7±5.4	3.6±1.4	−6.9±3.4	emi
292	38.86	−64.58	20.09	0.92	0.32430	0.00027	1.9± 2.6	1.6±2.4	4.2±1.1	1.5±4.0	abs
293	27.06	−64.30	21.61	1.01	0.33197	0.00020	1.3± 3.3	1.4±2.0	2.2±2.1	0.7±4.0	abs
295	−4.97	−61.35	20.18	0.96	0.32830	0.00027	0.1± 4.2	0.8±5.6	4.2±2.9	1.8±3.6	abs
298	−19.71	−58.77	19.46	1.03	0.32610	0.00027	−2.8±2.3	0.8±2.3	2.8±0.8	−0.7±6.0	abs
299	−45.12	−54.61	21.37	0.89	0.31510	0.00021	0.2± 4.0	1.5±2.4	1.2±0.9	4.4±3.6	abs
300	−14.97	−53.87	20.03	0.98	0.32160	0.00027	0.8± 2.1	2.6±2.8	1.8±1.8	−4.7±3.8	abs
303	−88.96	−53.79	20.04	0.98	0.32560	0.00027	0.9± 1.7	−1.6±2.9	2.8±1.5	0.0±4.3	abs
305	150.68	−48.39	21.00	0.86	0.33282	0.00020	3.6± 3.4	2.5±3.2	0.8±2.1	−5.5±5.3	emi
309	−26.33	−46.29	19.86	1.03	0.32470	0.00027	−1.2±2.2	2.2±4.1	1.9±1.1	···	abs
311	−2.50	−45.45	21.20	0.98	0.32700	0.00040	1.1± 7.0	7.3±7.2	4.2±3.1	−5.8±9.9	abs
318	212.54	−37.61	21.00	0.89	0.32728	0.00020	1.0± 3.6	3.5±4.1	3.9±1.4	−1.9±4.6	abs
319	29.68	−39.69	20.72	0.97	0.33440	0.00040	−0.6±4.6	2.5±6.7	3.5±3.2	2.1±5.0	abs
321	277.41	−35.51	20.08	···	0.32890	0.00020	3.7±1.8	2.6±3.2	3.2±1.6	2.9±2.0	abs
323	23.29	−38.10	21.11	0.90	0.33259	0.00020	0.5± 5.0	2.5±3.7	2.2±1.8	−1.6±13.9	abs
328	−4.03	−36.82	19.96	0.72	0.31757	0.00039	7.2± 1.3	6.6±2.2	3.8±2.1	−1.0±2.4	e+a
329	199.19	−34.23	20.72	0.93	0.32731	0.00020	0.8± 1.6	1.5±1.5	4.2±1.3	−0.6±4.4	abs
331	−146.58	−36.92	21.95	0.90	0.32493	0.00020	−5.0±5.3	1.2±4.2	1.2±2.1	−3.6±11.0	abs
335	9.21	−32.17	20.57	0.95	0.32240	0.00027	1.8± 3.9	3.2±3.5	2.1±2.4	−14.8±12.0	abs
343	−64.33	−25.27	20.64	0.78	0.32201	0.00027	5.3± 2.9	8.4±3.9	4.8±2.4	1.0±5.0	e+a
344	−38.25	−24.87	20.85	0.96	0.33330	0.00027	2.3± 4.3	2.7±8.2	5.0±2.9	−1.3±4.6	abs
346	−8.17	−23.07	19.78	0.89	0.32173	0.00020	2.2± 1.9	3.1±2.0	3.7±0.9	−0.8±2.4	abs
347	−51.92	−22.89	20.13	0.97	0.32790	0.00040	4.2± 3.1	−0.7±3.4	−0.2±2.7	1.0±5.6	abs
348	242.81	−18.89	20.50	0.94	0.33336	0.00020	−0.3±3.9	−2.6±3.1	2.8±2.5	0.2±5.1	abs
349	63.65	−19.66	21.47	0.93	0.32840	0.00040	4.4± 6.9	−0.9±11.2	2.6± 3.2	1.2±5.6	abs
350	−9.53	−20.00	21.06	0.97	0.32280	0.00040	3.5± 4.5	0.4±12.9	2.1± 1.7	6.4±3.0	abs
351	−109.02	−21.23	20.10	0.72	0.33300	0.00040	3.5± 2.4	1.4±3.7	−0.3±2.0	−6.5±2.1	emi
352	−6.09	−17.74	20.95	1.01	0.32780	0.00040	−0.9±8.5	2.9±9.4	−1.7±4.2	9.5±4.8	abs
353	7.80	−17.57	19.42	1.03	0.32367	0.00041	−0.9±1.3	2.1±2.0	1.8±0.8	0.7±1.8	abs
354	3.73	−16.28	20.98	1.00	0.32372	0.00028	4.6± 4.7	3.3±4.1	1.8±2.2	−4.9±6.3	abs
356	−23.23	−11.19	19.68	1.06	0.34000	0.00040	2.7± 6.2	−5.3±7.2	2.6±3.7	−20.2±15.2	abs
357	−1.58	−10.79	20.83	0.98	0.32790	0.00040	5.4± 8.4	0.8±15.5	−3.8± 4.9	−11.2±9.1	abs
358	4.91	−10.15	20.83	0.99	0.32510	0.00040	−2.0±4.7	−4.2±6.9	4.9±2.4	8.8±5.3	abs
359	66.68	−9.02	19.91	0.97	0.32470	0.00027	−0.1±1.2	2.7±1.6	3.1±0.9	2.5±3.0	abs
360	1.76	−9.25	20.62	0.98	0.32297	0.00020	1.3± 2.4	1.1±2.6	3.1±1.4	−0.1±3.0	abs
361	56.87	−8.42	21.03	0.94	0.33140	0.00040	−5.6±3.6	3.7±7.4	1.6±2.9	···	abs
362	305.72	−4.20	20.66	···	0.32789	0.00024	4.7±1.8	3.9±1.6	−2.0±1.5	−24.7±2.0	emi+Hδ
366	137.90	−4.65	20.25	1.00	0.32368	0.00020	0.8± 2.6	3.2±2.5	3.3±1.5	−0.4±4.0	abs
368	0.78	−5.02	20.31	1.01	0.32861	0.00059	−0.5±2.9	1.1±2.9	4.1±1.4	−0.2±3.9	abs
369	122.54	−3.36	20.42	0.96	0.32076	0.00020	1.4± 2.9	1.6±3.1	2.7±1.6	−6.1±3.9	emi

TABLE 1—*Continued*

Num	x(″)	y(″)	R	$V-R$	z	$\varepsilon(z)$	Hδ	Hγ	Hβ	[OII]	Notes
371	87.25	−2.90	19.71	1.02	0.33257	0.00039	−1.3±1.5	−0.7±2.5	3.0±1.3	−2.1±2.0	abs
372	−103.57	−3.81	20.07	0.91	0.32035	0.00051	0.5± 3.0	0.9±2.3	3.4±1.4	1.4±2.0	abs
375	0.00	0.00	19.09	1.04	0.32750	0.00040	−2.9±3.9	1.4±3.9	2.6±2.3	−11.3±4.1	bcg+emi
376	54.14	1.47	20.48	1.00	0.32150	0.00027	0.1± 2.7	2.1±5.0	2.5±1.3	···	abs
377	184.21	3.80	20.40	0.69	0.32355	0.00020	3.5± 3.2	4.0±4.1	0.8±2.5	−6.7±3.5	emi
380	−27.82	4.98	20.80	0.54	0.32660	0.00040	5.1±2.6	5.8±5.6	0.0±3.4	−11.3±5.6	emi+Hδ
381	−0.06	6.01	19.91	0.98	0.32580	0.00027	0.8±2.7	2.9±4.5	2.6±1.7	2.7±3.9	abs
383	10.29	7.60	21.23	0.97	0.33580	0.00104	−0.3±2.9	3.1±5.9	0.6±2.4	0.3±2.7	abs
386	−2.73	8.27	20.68	1.11	0.32210	0.00020	−6.4±5.9	−0.4±6.5	3.9±3.7	6.3±5.3	abs
388	−63.65	12.02	21.95	0.93	0.32599	0.00020	−0.4±5.2	−1.7±4.3	2.0±2.9	1.2±4.7	abs
391	−18.77	13.22	19.81	0.99	0.32370	0.00027	−0.1±4.2	0.2±4.1	0.6±1.9	0.1±4.7	abs
394	110.45	20.22	21.34	0.96	0.32623	0.00028	0.6±4.2	2.4±4.4	1.0±1.9	2.4±12.7	abs
396	−66.44	18.82	20.95	0.51	0.31930	0.00027	4.0±2.0	−3.4±4.4	−14.0±3.0	−47.7±6.9	emi+Hδ
397	−82.60	19.35	20.61	0.96	0.32210	0.00027	−2.8±3.0	1.4±3.0	3.8±1.6	4.9±4.5	abs
399	246.83	25.25	20.49	0.64	0.32404	0.00023	6.6±2.0	3.3±1.6	−1.2±1.6	−11.9±2.1	emi+Hδ
400	53.22	22.94	21.54	0.94	0.32600	0.00040	7.2±9.7	0.4±12.9	2.5±3.2	16.5±11.8	abs
406	−121.17	24.15	21.82	0.88	0.32840	0.00030	3.0±6.5	4.0±2.8	2.4±4.2	−1.9±6.3	abs
408	−5.33	25.92	20.25	0.99	0.31961	0.00041	−2.0±2.6	0.8±3.3	3.0±1.3	0.2±2.5	abs
409	−90.55	25.48	21.16	0.99	0.32940	0.00040	−2.7±5.6	2.6±8.3	3.5±3.4	4.2±4.9	abs
410	49.29	30.66	20.70	1.03	0.33000	0.00027	−3.4±2.7	1.2±2.9	2.1±1.2	0.8±2.2	abs
411	115.12	31.73	21.04	1.01	0.32110	0.00040	4.0±3.1	0.3±5.3	3.3±2.2	3.8±5.8	abs
412	−78.28	30.39	20.44	0.91	0.31780	0.00040	−0.1±4.2	2.3±5.3	6.2±3.1	−0.7±3.0	abs
416	2.95	33.74	21.52	1.06	0.32165	0.00020	−0.1±4.0	1.9±3.8	1.2±2.5	4.5±6.8	abs
420	−18.87	36.69	21.97	0.74	0.31904	0.00020	3.2±3.4	5.9±3.8	5.7±3.0	1.0±6.4	e+a
421	−32.31	37.35	20.83	1.04	0.33150	0.00040	−1.7±2.4	0.5±5.1	2.9±1.4	−1.6±4.7	abs
430	−273.20	39.29	20.72	0.90	0.32630	0.00022	2.3±5.2	2.1±4.3	5.9±4.2	−0.6±2.2	abs
433	52.28	43.85	20.16	0.96	0.32601	0.00059	−1.3±2.7	0.1±2.8	3.6±1.3	1.5±1.8	abs
434	1.34	45.48	21.59	1.01	0.33611	0.00020	−1.8±1.9	0.5±2.9	2.5±1.8	−2.1±4.0	abs
440	−120.58	49.83	21.05	0.97	0.32929	0.00020	0.8±4.7	0.7±2.1	3.1±1.3	−0.1±4.8	abs
442	14.85	52.33	21.20	0.92	0.32251	0.00020	0.9±4.6	4.1±5.1	0.9±1.8	7.7±7.8	abs
444	154.20	56.42	20.29	1.04	0.33078	0.00020	0.4±2.8	1.8±2.6	1.9±1.2	−1.5±4.9	abs
447	164.96	57.93	20.73	0.99	0.32906	0.00020	1.5±2.3	3.0±3.3	1.6±1.8	1.6±3.5	abs
452	−197.18	55.21	20.39	0.97	0.33020	0.00020	0.4±2.5	0.4±2.8	3.2±1.4	−1.8±4.5	abs
453	194.73	63.33	20.40	0.56	0.32083	0.00020	6.1±2.5	3.8±1.9	−8.6±2.2	−40.1±4.6	emi+Hδ
454	46.57	61.96	19.89	0.96	0.32750	0.00027	1.8±2.3	2.0±4.0	3.7±1.5	−0.8±1.7	abs
457	−143.89	63.30	21.02	0.99	0.33043	0.00020	3.9±3.7	−0.5±2.5	2.6±0.8	−3.3±7.1	abs
460	51.45	70.69	21.36	1.00	0.33216	0.00020	0.5±2.9	−0.4±3.9	2.8±1.6	−1.2±4.4	abs
463	8.03	75.87	19.91	0.99	0.32797	0.00059	1.1±1.6	1.7±2.9	2.3±1.5	3.7±2.4	abs
465	3.38	76.79	20.53	1.00	0.33050	0.00040	3.7±2.7	−0.7±8.2	4.5±2.3	−13.8±13.5	abs
468	171.80	83.16	20.52	1.02	0.33242	0.00020	1.8±1.9	−1.5±3.1	2.3±1.6	−0.9±3.1	abs
469	225.73	84.35	21.51	0.85	0.32679	0.00020	3.4±4.1	−0.9±2.9	1.8±2.2	−0.6±4.2	abs
470	131.21	84.61	19.50	1.01	0.33383	0.00020	0.0±2.8	−0.2±1.8	3.2±0.9	−0.8±1.9	abs
473	47.42	87.30	21.04	0.89	0.33335	0.00020	2.8±3.0	0.8±5.1	3.1±2.0	1.2±5.5	abs
481	−44.17	91.14	21.24	0.95	0.33101	0.00064	4.1±4.1	4.2±3.9	4.4±2.4	6.9±3.6	e+a
482	40.83	94.80	21.28	1.05	0.32481	0.00020	1.6±3.3	3.2±3.6	2.7±1.1	0.3±2.5	abs
491	239.36	101.40	20.50	0.88	0.32677	0.00020	2.1±1.9	0.4±1.3	−0.9±1.0	−12.4±1.4	emi
492	110.31	99.96	20.61	1.04	0.33464	0.00020	2.4±1.7	3.0±2.0	3.0±1.2	−2.6±3.2	abs
493	11.71	98.91	21.70	1.01	0.33082	0.00020	3.1±3.3	3.4±3.5	3.5±2.1	−1.2±3.2	abs
498	67.82	106.81	21.28	0.98	0.33029	0.00020	4.3±6.0	−2.1±5.2	3.2±1.5	2.7±10.0	abs
507	−181.26	112.42	20.45	0.81	0.32387	0.00020	3.7±1.9	5.8±2.6	4.1±2.1	−1.7±2.5	e+a
510	55.50	117.34	20.50	0.97	0.33322	0.00020	2.5±1.1	2.4±1.4	3.2±1.1	−1.4±2.1	abs
514	−58.30	119.21	21.06	0.90	0.33070	0.00020	2.6±2.7	1.1±1.1	2.8±1.4	4.0±3.1	abs
519	−32.42	124.38	20.84	0.66	0.32390	0.00020	0.2±1.5	0.3±1.7	−12.3±1.7	−41.1±3.6	emi
522	−125.36	124.35	21.44	0.90	0.33011	0.00020	3.5±4.2	0.0±5.8	4.8±4.4	−0.1±5.7	abs
523	37.47	126.64	20.21	1.07	0.32323	0.00020	1.0±3.3	−1.5±4.5	3.3±1.8	1.0±2.8	abs
525	−137.72	125.54	20.48	0.96	0.33137	0.00020	1.1±2.5	0.3±1.9	3.3±1.1	−0.1±3.0	abs
528	−17.83	132.87	20.78	0.55	0.32373	0.00020	4.9±1.6	2.5±1.8	−6.8±1.9	−46.0±3.6	emi+Hδ

TABLE 1—*Continued*

Num	x(″)	y(″)	R	$V-R$	z	$\varepsilon(z)$	Hδ	Hγ	Hβ	[OII]	Notes
531	−68.80	136.31	19.21	1.02	0.33075	0.00020	0.5±1.0	−0.6±1.8	2.4±0.8	1.2±1.5	abs
534	−124.68	140.37	20.83	0.97	0.32356	0.00020	−1.3±3.8	2.2±2.8	2.1±1.9	−1.0±3.5	abs
536	17.01	144.87	19.34	1.02	0.32789	0.00020	−0.2±1.0	0.6±1.3	2.1±0.9	1.1±1.6	abs
537	31.69	145.16	20.66	0.98	0.32602	0.00020	−0.5±2.0	1.7±2.3	1.2±1.0	−0.2±1.8	abs
539	108.68	146.75	21.20	1.03	0.32589	0.00020	1.7±4.1	3.1±3.9	2.2±1.7	0.5±6.1	abs
540	68.26	147.10	20.87	1.00	0.32781	0.00020	2.3±2.7	−1.0±2.4	1.9±1.5	−3.3±3.9	abs
542	−4.28	150.03	20.23	1.00	0.33162	0.00020	0.4±1.3	0.2±2.1	3.1±1.1	1.2±2.2	abs
544	−195.75	151.37	20.42	1.06	0.33280	0.00020	−0.3±2.0	0.0±2.2	2.6±1.3	−1.4±2.3	abs
546	100.43	157.41	20.96	0.93	0.33118	0.00020	−0.4±3.1	2.7±2.3	2.8±2.5	2.6±2.7	abs
549	47.65	161.11	20.55	0.91	0.33281	0.00020	2.6±2.2	2.3±2.3	2.7±2.0	−1.5±1.9	abs
553	−150.30	160.49	21.55	0.84	0.31894	0.00024	5.6±3.6	3.3±4.3	2.1±2.3	−2.4±6.0	abs
554	−252.31	160.29	19.95	1.00	0.32971	0.00020	−0.3±1.4	0.4±1.5	2.7±0.8	−0.3±1.6	abs
555	82.82	164.56	21.48	1.00	0.32956	0.00020	3.1±2.0	0.5±3.1	3.4±1.8	1.6±5.3	abs
560	21.67	170.53	20.41	0.99	0.33136	0.00020	1.6±1.1	0.5±1.9	2.4±0.9	−1.2±2.1	abs
562	57.01	175.13	20.91	0.73	0.33643	0.00020	6.2±4.5	1.1±5.1	7.0±4.6	0.6±5.3	e+a
565	140.21	177.65	21.78	0.80	0.32449	0.00030	5.6±4.2	4.4±4.5	4.7±3.5	2.5±5.2	e+a
572	−198.72	181.74	20.25	0.94	0.33287	0.00020	1.4±0.8	0.3±2.3	1.9±1.0	−3.1±3.0	abs
584	−54.21	201.30	21.36	0.97	0.32949	0.00033	−1.7±4.5	1.8±3.8	1.8±1.9	−2.2±9.9	abs
587	43.66	206.78	21.61	0.82	0.33483	0.00035	4.1±3.2	2.4±2.0	2.0±2.4	−5.8±7.0	abs
591	−204.21	209.09	21.81	0.63	0.33451	0.00020	4.8±4.7	8.1±4.3	−1.7±5.0	−18.1±9.1	emi+Hδ
594	−169.55	213.66	21.85	0.70	0.33453	0.00032	10.3±2.0	4.5±1.1	3.6±3.0	−9.4±4.5	emi+Hδ
595	261.33	219.25	19.52	···	0.33694	0.00020	4.1±0.7	1.6±0.8	−5.7±1.0	−22.5±1.3	emi+Hδ
599	237.32	224.40	20.65	···	0.33514	0.00020	−0.2±2.3	1.7±2.8	2.5±1.5	0.4±2.2	abs
604	−223.01	221.73	20.40	0.93	0.32494	0.00020	0.8±3.2	0.3±2.1	2.5±1.7	−1.4±4.1	abs
626	−56.50	255.17	20.38	1.01	0.33207	0.00020	1.1±3.8	−0.3±3.7	2.8±2.1	2.0±4.5	abs
636	31.61	270.99	20.83	···	0.32433	0.00020	4.4±3.0	2.7±5.2	3.6±5.2	−8.4±3.5	emi+Hδ
647	140.31	280.70	20.24	0.94	0.33096	0.00020	2.4±2.1	1.6±1.7	3.0±1.1	−2.2±3.1	abs
649	−269.81	278.28	19.99	···	0.32803	0.00020	0.9±2.5	0.1±2.8	3.3±1.4	2.6±3.6	abs
652	205.97	286.74	21.39	···	0.33304	0.00082	3.1±5.0	0.6±4.4	−0.2±2.6	−24.5±6.5	emi
1155	173.49	−253.08	22.90	···	0.33406	0.00020	···	···	···	−47.4±23.7	emi
1157	35.80	−254.31	21.83	···	0.33328	0.00020	−2.1±2.8	−1.6±5.3	2.5±2.6	−3.1±7.0	abs
1188	−88.63	−238.14	22.08	0.75	0.32222	0.00029	3.9±6.4	−1.5±6.2	−3.5±4.2	−6.7±5.8	emi
1195	108.86	−228.36	22.90	0.33	0.32956	0.00021	11.5±11.9	3.2±15.5	−3.4± 6.0	−34.8±11.4	emi
1328	−192.34	−159.57	21.86	1.00	0.33102	0.00020	2.3±3.4	−0.1±3.4	2.0±2.8	1.9±5.7	abs
1341	−242.25	−150.00	22.40	0.51	0.32058	0.00047	5.1±5.3	2.9±5.8	0.3±4.2	−30.7±7.5	emi
1352	−139.82	−144.49	21.91	0.80	0.32833	0.00022	4.1±4.3	0.4±4.9	3.1±3.2	7.9±9.3	abs
1414	116.29	−115.11	21.98	0.94	0.33304	0.00020	3.9±5.1	4.8±7.4	−0.6±3.9	−1.6±6.1	abs
1455	−3.46	−89.39	22.13	0.90	0.33028	0.00020	−2.2±5.4	2.2±5.3	2.8±3.1	−0.3±7.2	abs
1461	97.04	−83.36	22.29	0.71	0.32747	0.00032	−3.4±9.7	4.0±7.3	6.2±5.8	7.7±14.1	abs
1475	−19.94	−76.88	20.57	···	0.33191	0.00020	2.0±1.6	2.6±2.5	2.2±1.1	2.1±1.6	abs
1487	139.12	−58.63	23.08	0.41	0.32081	0.00020	10.6± 15.5	3.7±17.4	−19.9±30.7	−43.9±8.8	emi
1524	82.16	−39.65	21.86	0.98	0.33574	0.00020	−0.5±3.5	2.2±3.7	1.3±4.1	−0.6±4.4	abs
1563	−62.95	−23.67	21.47	···	0.33136	0.00020	−0.2± 3.8	−3.7±5.4	3.5±2.3	3.1±7.7	abs
1594	−21.42	−14.73	22.04	···	0.32330	0.00024	−4.8±15.6	−18.6±19.2	6.2±13.6	3.0±10.9	abs
1604	95.36	−5.09	22.54	0.91	0.32662	0.00027	4.5± 14.2	−7.2±12.8	1.4± 7.2	−2.9±18.4	abs
1616	30.67	−1.91	22.02	1.01	0.33368	0.00020	2.9±2.9	3.7±4.3	2.4±2.6	3.8±4.9	abs
1630	92.41	12.82	22.15	0.62	0.33221	0.00020	8.2±4.6	−3.5±6.0	−5.2±2.8	−29.3±7.5	emi+Hδ
1649	71.56	20.50	21.62	0.97	0.32544	0.00020	2.4±3.7	2.0±3.1	1.3±4.0	3.2±3.2	abs
1731	−75.92	67.56	21.84	0.82	0.32830	0.00020	−0.8±3.6	3.7±2.7	2.5±2.4	3.5±3.6	abs
1775	116.86	97.78	21.65	0.88	0.33430	0.00027	10.5±7.6	2.5±9.4	−1.9±6.2	−0.1±9.9	abs
1806	93.60	118.92	21.75	1.08	0.33190	0.00020	3.4±3.0	−9.0±4.3	1.3±3.6	2.9±7.7	abs
1810	275.48	122.77	22.21	···	0.32758	0.00023	6.5± 10.6	−8.5±8.2	−8.4±5.2	−56.6±12.4	emi
1816	77.81	123.90	22.21	0.82	0.33413	0.00020	−1.0±4.2	2.6±4.3	0.0±4.3	−3.8±14.7	abs
1829	136.67	131.11	23.03	0.76	0.33386	0.00020	2.4± 13.2	−0.5±9.6	−4.1±10.8	−27.6±25.9	emi
1842	−14.42	133.77	22.09	0.86	0.32299	0.00024	4.1±6.2	−2.7±6.5	0.0±5.2	−4.2±9.3	abs
1859	−76.77	142.06	21.99	0.96	0.33254	0.00020	2.6±4.1	3.2±2.5	2.6±4.1	3.8±5.4	abs
1865	111.08	146.35	21.43	···	0.32847	0.00020	−1.2±8.8	−2.8±9.0	4.8±6.0	−5.0±10.7	abs

TABLE 1—*Continued*

Num	x(″)	y(″)	R	$V-R$	z	$\varepsilon(z)$	Hδ	Hγ	Hβ	[OII]	Notes
1871	16.32	147.17	20.37	···	0.32681	0.00020	0.1±1.7	0.8±2.1	2.6±1.0	0.3±1.5	abs
1897	138.96	166.83	21.67	0.79	0.33097	0.00024	2.7±7.0	1.9±4.6	2.3±3.4	−0.3±14.4	abs
1978	140.46	229.01	22.31	1.04	0.33076	0.00024	2.1±9.9	3.3±10.8	2.1±7.4	−11.1±29.8	abs
2081	−103.05	281.87	22.36	0.45	0.33467	0.00077	−8.8±18.7	1.9±13.8	−14.0±20.7	−65.4±22.3	emi

TABLE 2
LINE STRENGTH INDEX DEFINITIONS

Index	Bandpass	Blue sideband	Red sideband
Hδ	4083.500−4122.250	4017.00−4057.00	4153.00−4193.00
Hγ	4319.750−4363.500	4242.00−4282.00	4404.00−4444.00
Hβ	4847.875−4876.625	4799.00−4839.00	4886.00−4926.00
[OII]	3716.300−3738.300	3696.30−3716.30	3738.30−3758.30

TABLE 3
SPECTRAL TYPE KINEMATICS

Type	Num	Mean	Dispersion
All	232	98425±90	1027^{+51}_{-45}
Absorption	177	98464±97	972^{+56}_{-48}
E+A	11	97891±567	1414^{+463}_{-234}
Emission	44	98402±228	1136^{+146}_{-105}
Emi (<20Å)	23	98419±303	1092^{+211}_{-134}
Emi (>20Å)	21	98383±352	1210^{+248}_{-154}
Emi+Hδ	16	98059±419	1260^{+312}_{-179}

NOTE.—Kinematic parameters as a function of spectral type. The emission-line galaxy spectra have been subdivided into those showing moderate (5 Å≤ [OII] 3727 Å≤20 Å) and strong ([OII] 3727 Å≥20 Å) emission and those with strong Hδ absorption (≥4 Å) irrespective of [OII] strength.

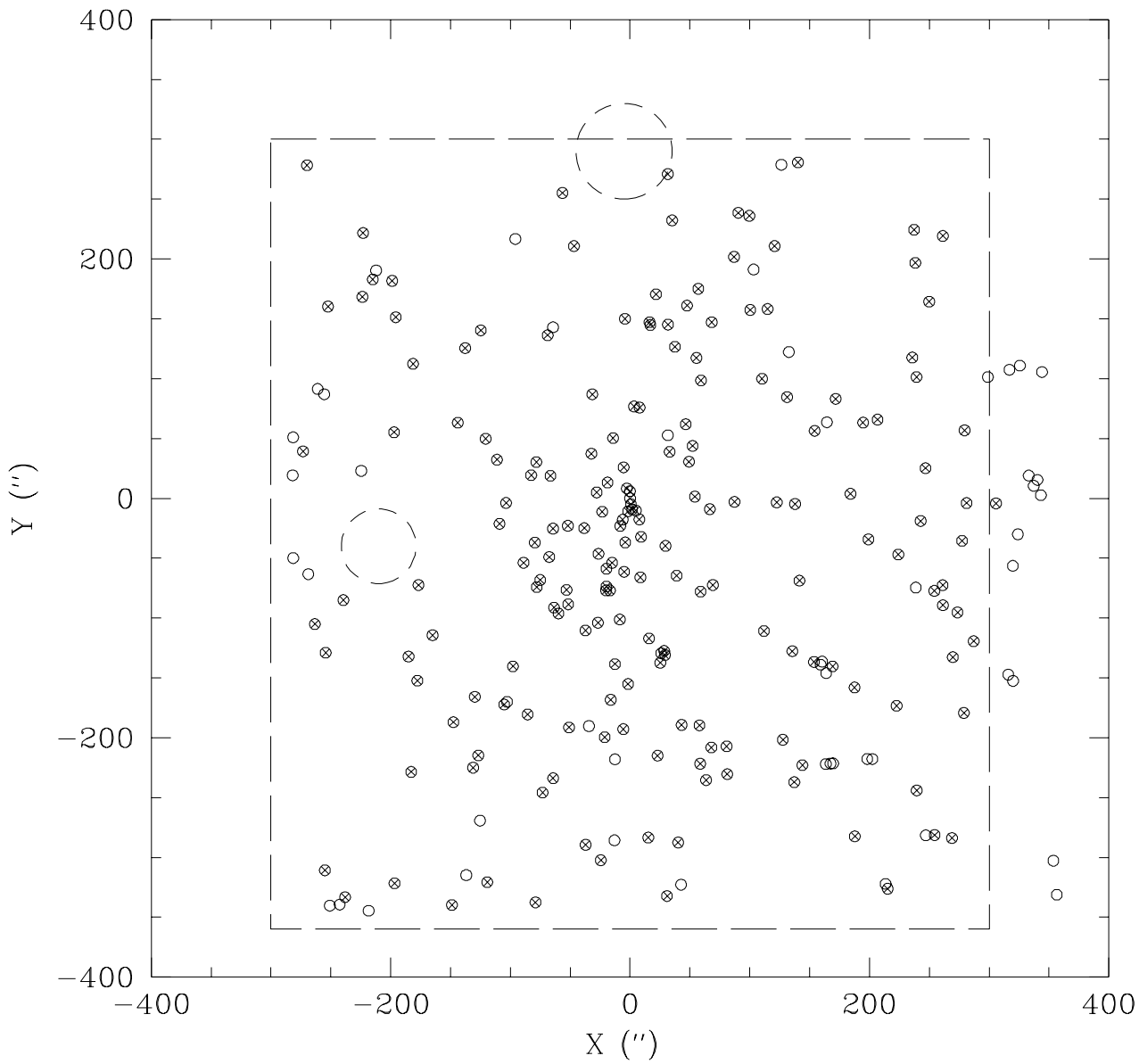
400
200
0
−200
−400
Y (″)
−400
−200
0
200
400
X (″)

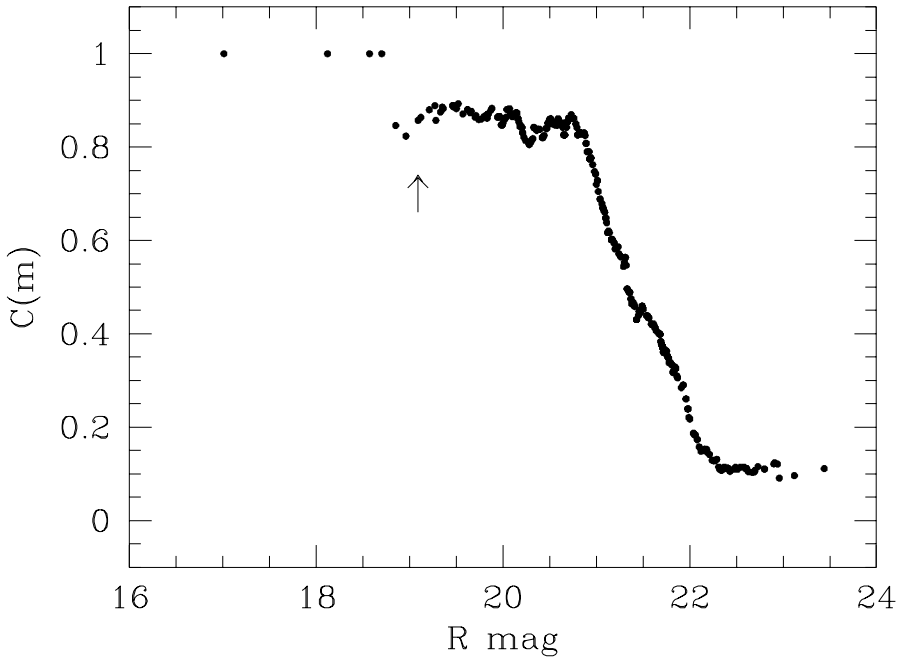
1
0.8
0.6
0.4
0.2
0
C(m)
16
18
20
22
24
R mag

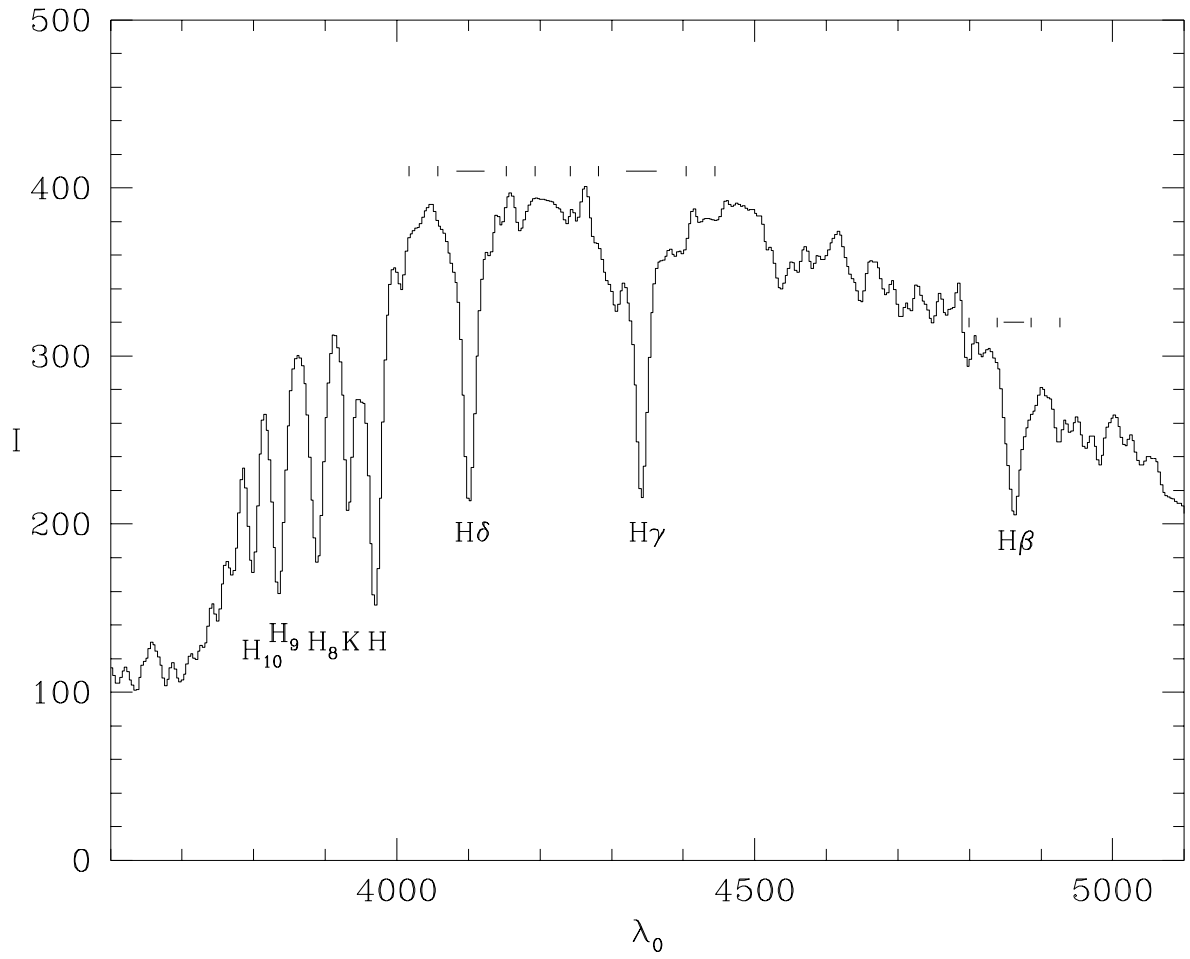
500
400
300
200
100
0
I
4000
4500
5000
λ_0
H_{10}
H_9
H_8
K
H
Hδ
Hγ
Hβ

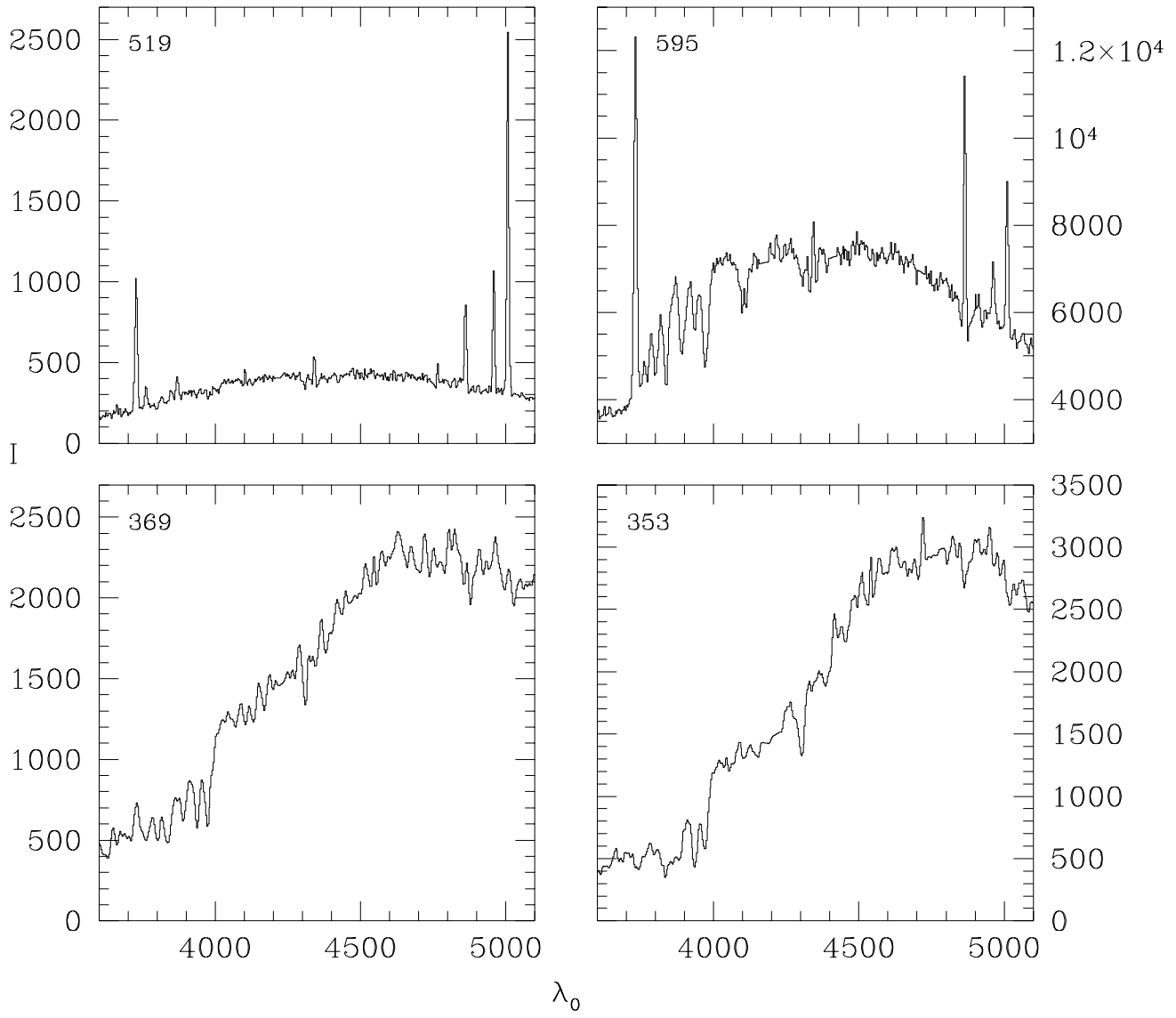
519
595
369
353
I
λ_0
2500
2000
1500
1000
500
0
1.2×10^4
10^4
8000
6000
4000
3500
3000
4000
4500
5000

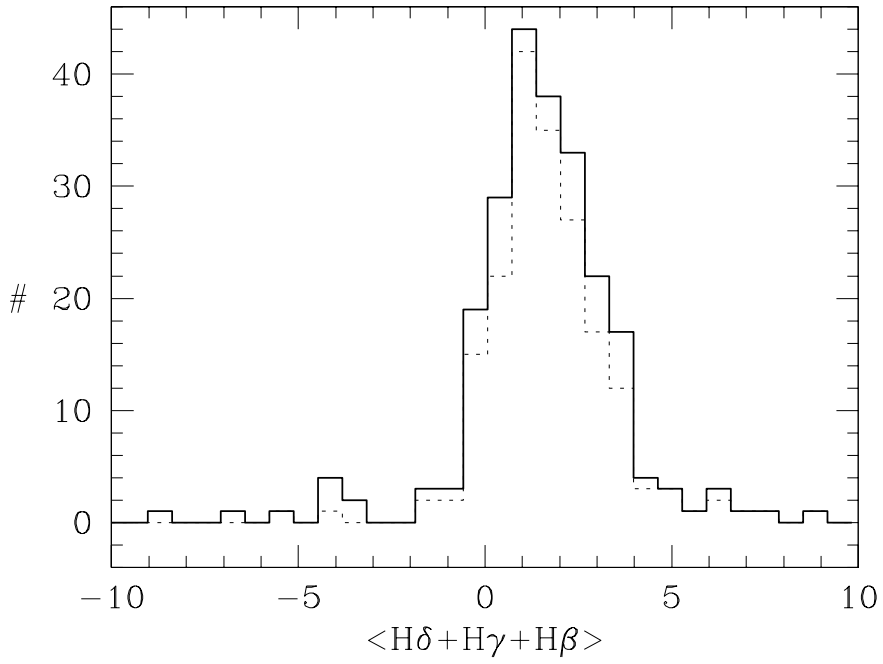
40
30
20
10
0
−10
−5
0
5
10
<Hδ+Hγ+Hβ>

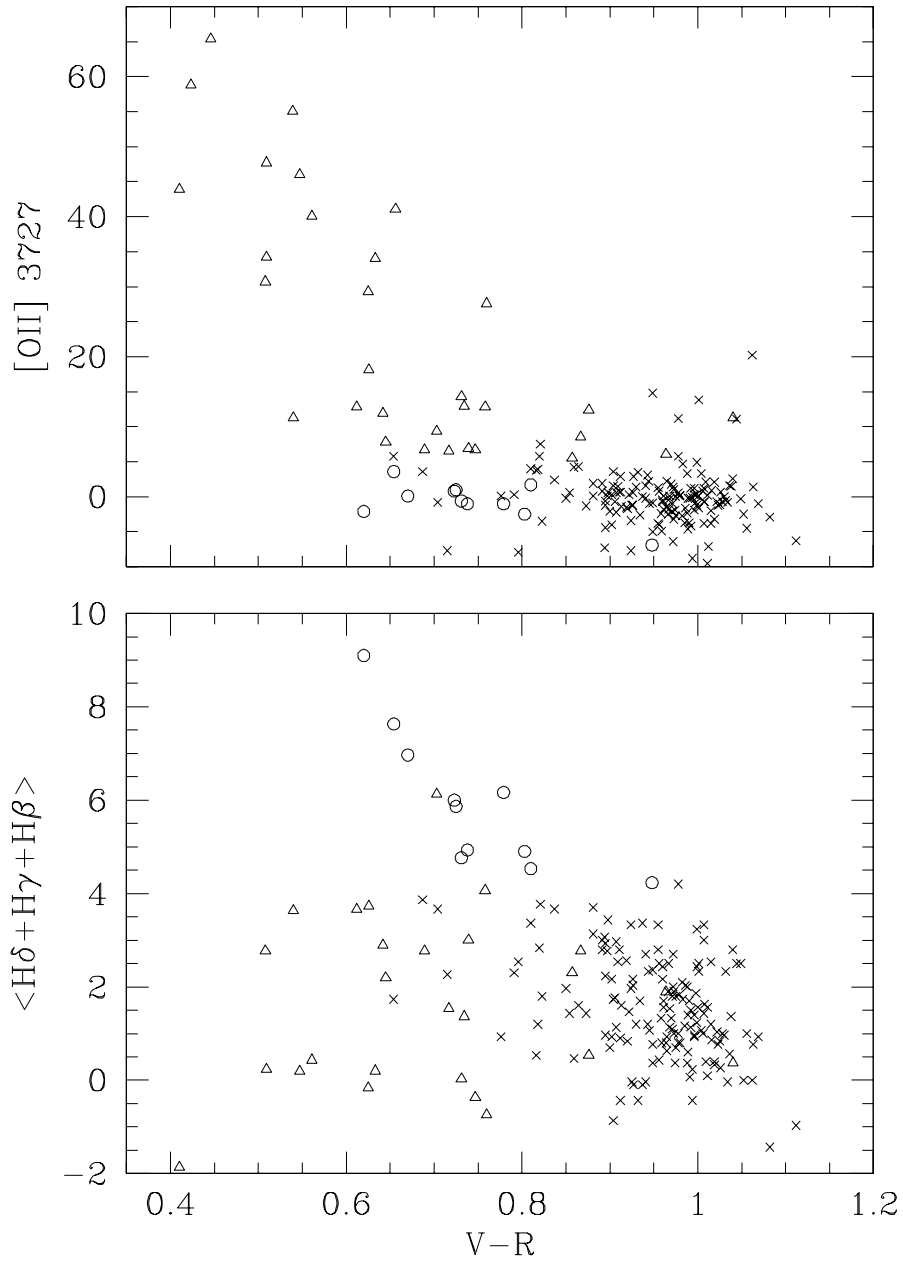
[OII] 3727
60
40
20
0
<Hδ+Hγ+Hβ>
10
8
6
4
2
0
−2
0.4
0.6
0.8
1
1.2
V−R

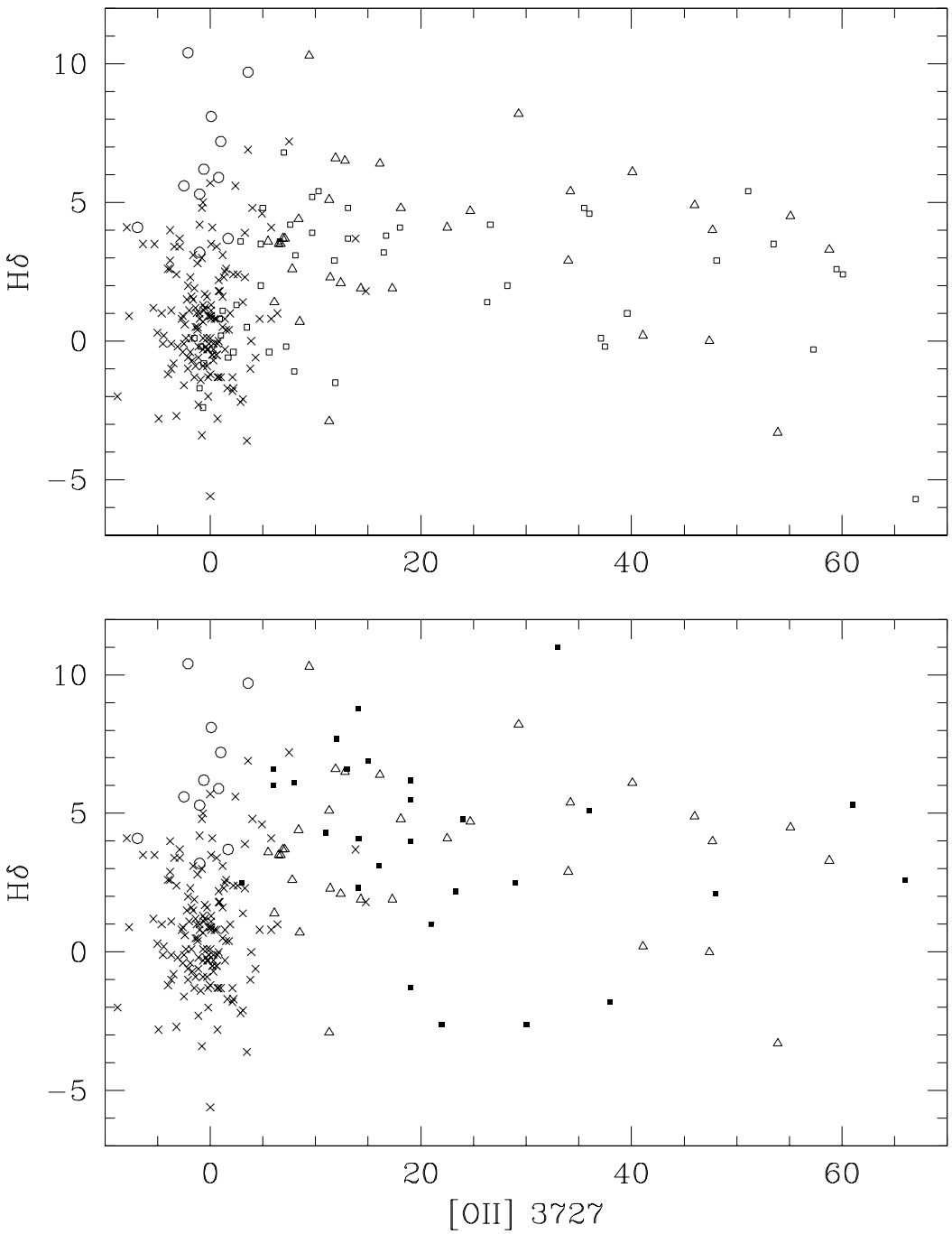
10
5
0
−5
Hδ
0
20
40
60
10
5
0
−5
Hδ
0
20
40
60
[OII] 3727

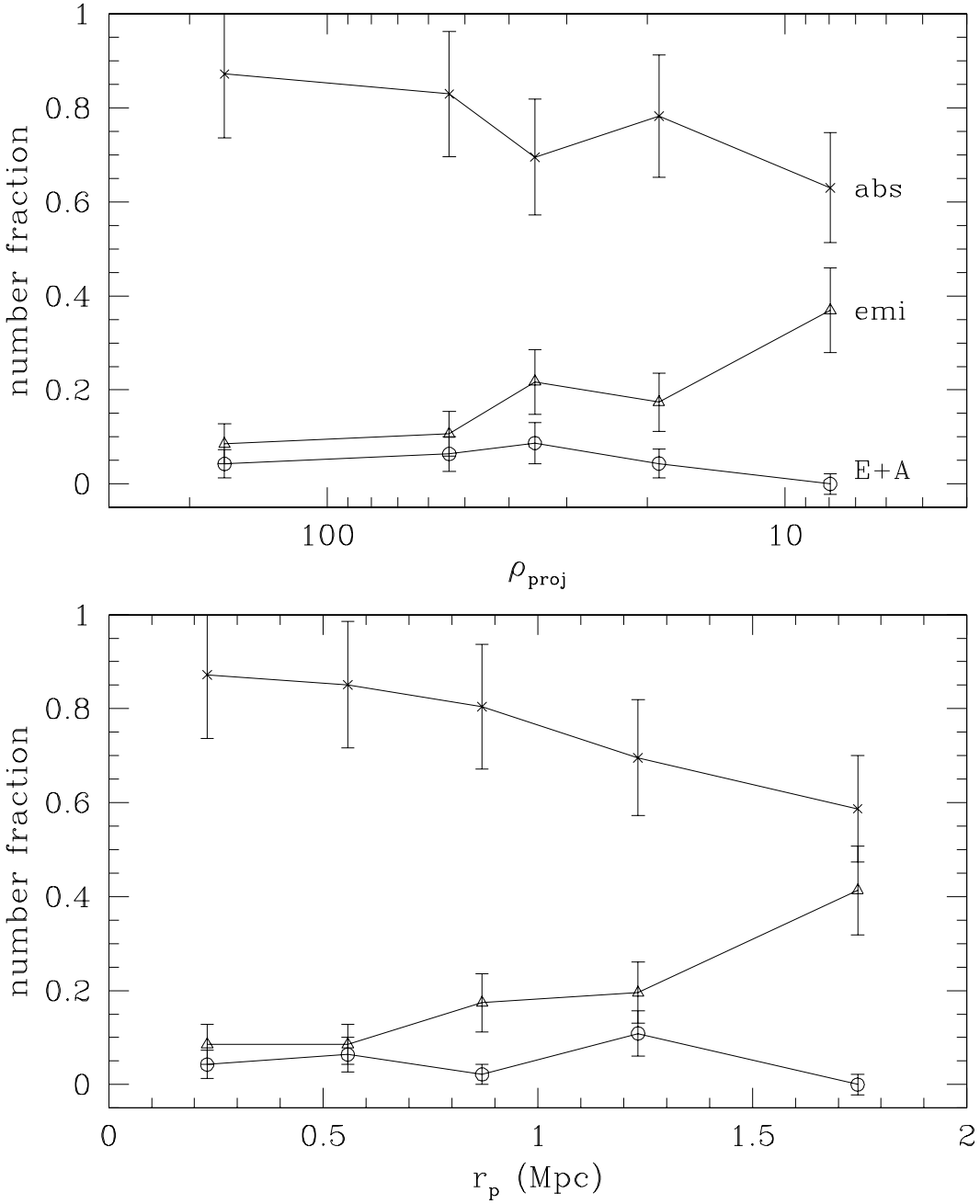
number fraction
1
0.8
0.6
0.4
0.2
0
abs
emi
E+A
100
10
$\rho_{\rm proj}$
number fraction
1
0.8
0.6
0.4
0.2
0
0
0.5
1
1.5
2
r_p (Mpc)

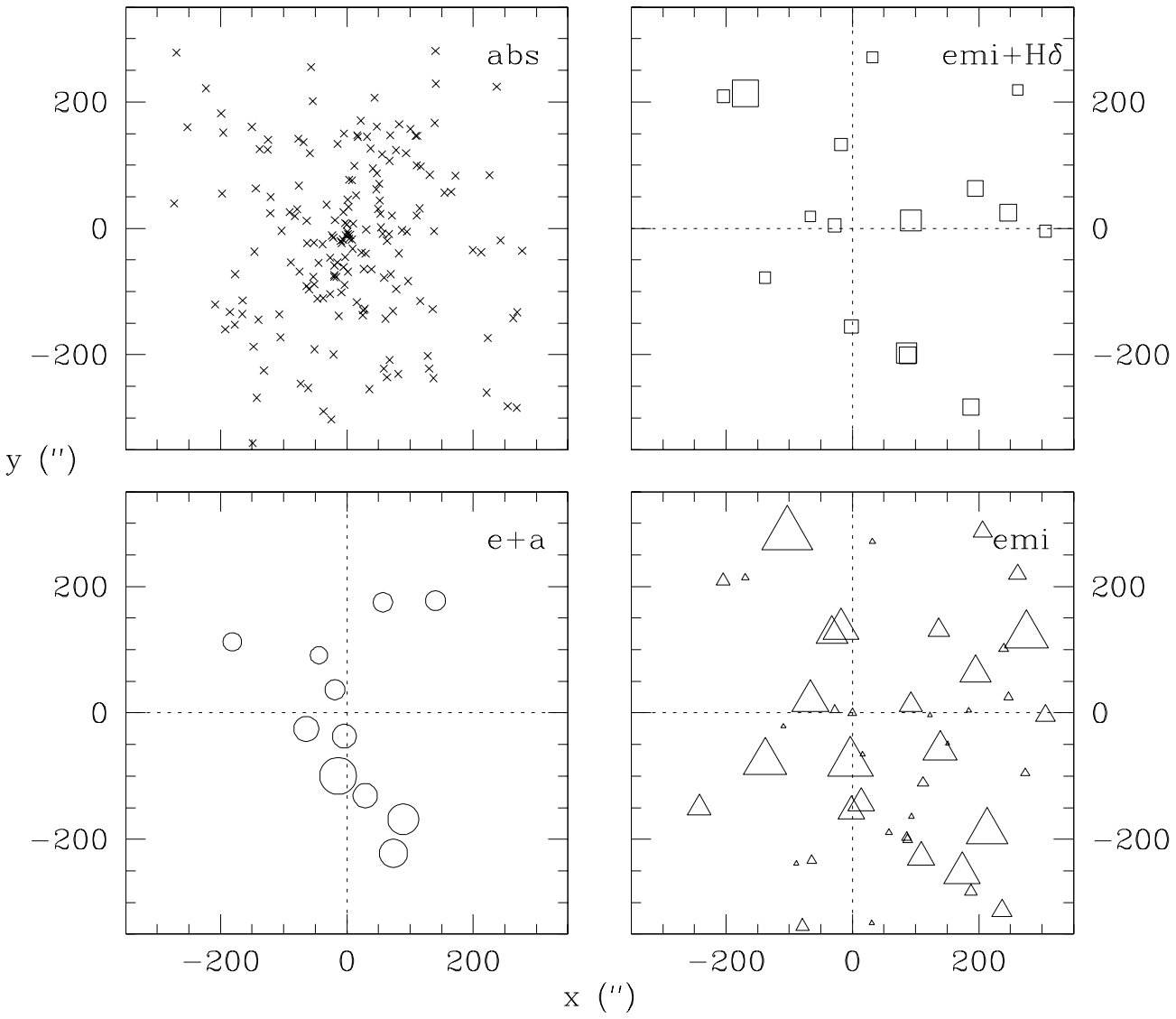
abs
emi+Hδ
e+a
emi
200
0
−200
y (″)
x (″)

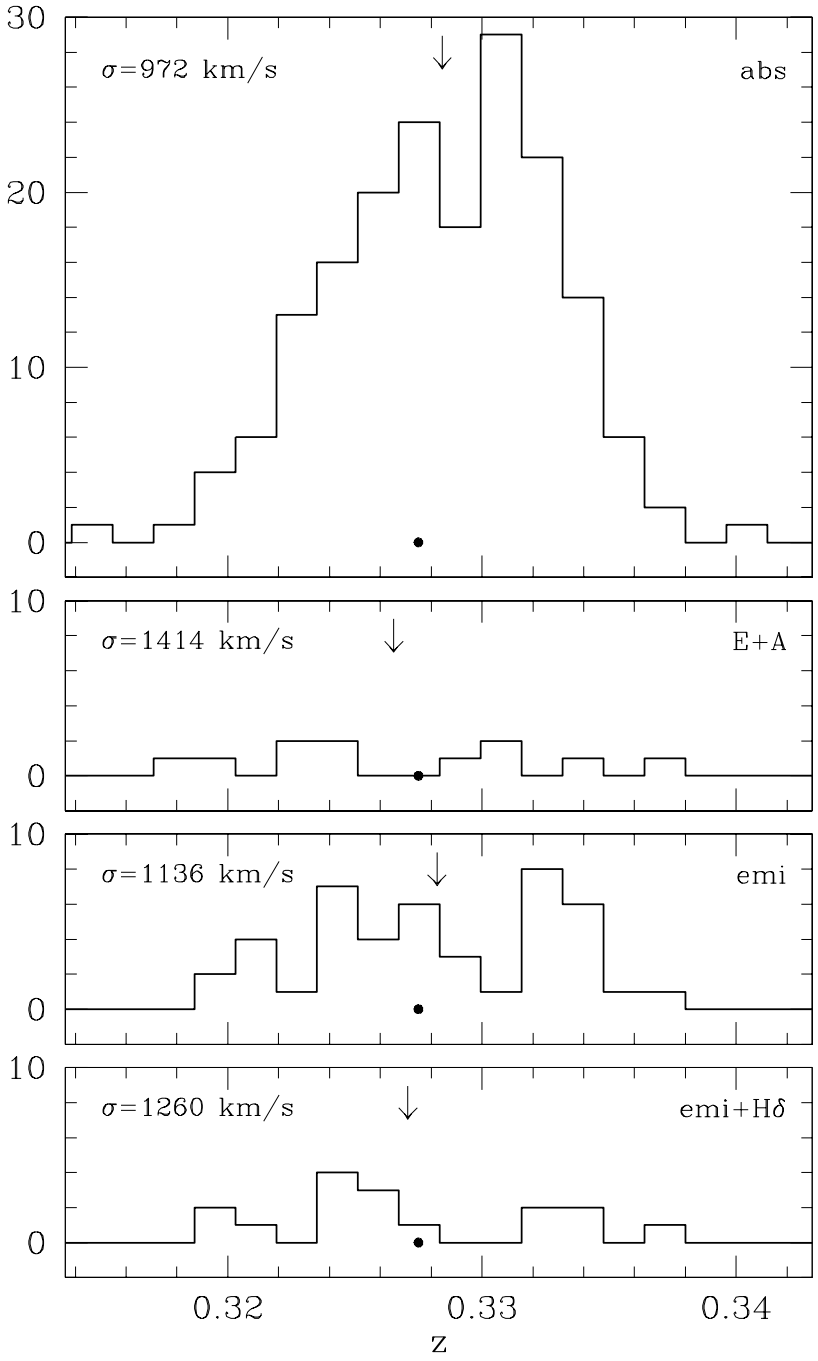
30
20
10
0
σ=972 km/s
abs
10
0
σ=1414 km/s
E+A
10
0
σ=1136 km/s
emi
10
0
σ=1260 km/s
emi+Hδ
0.32
0.33
0.34
z

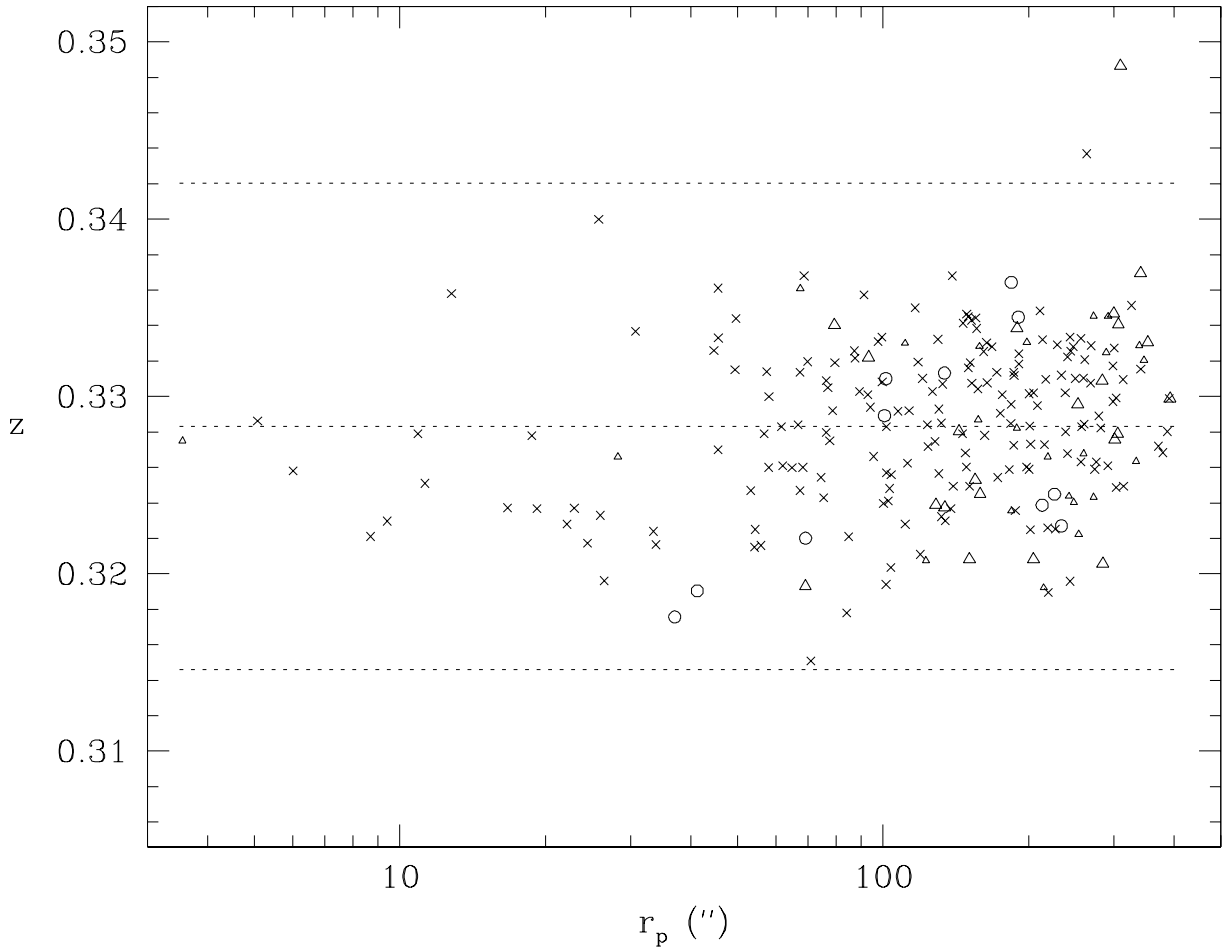
0.35
0.34
0.33
0.32
0.31
z
10
100
r_p ($''$)

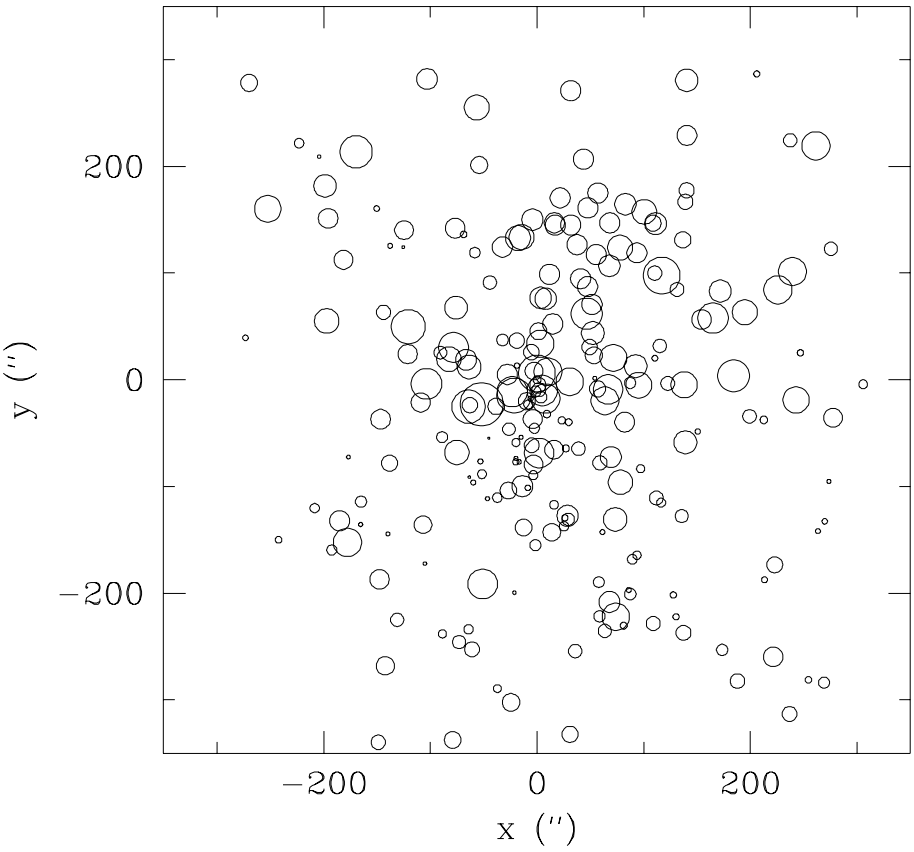
200
0
−200
y (″)
−200
0
200
x (″)

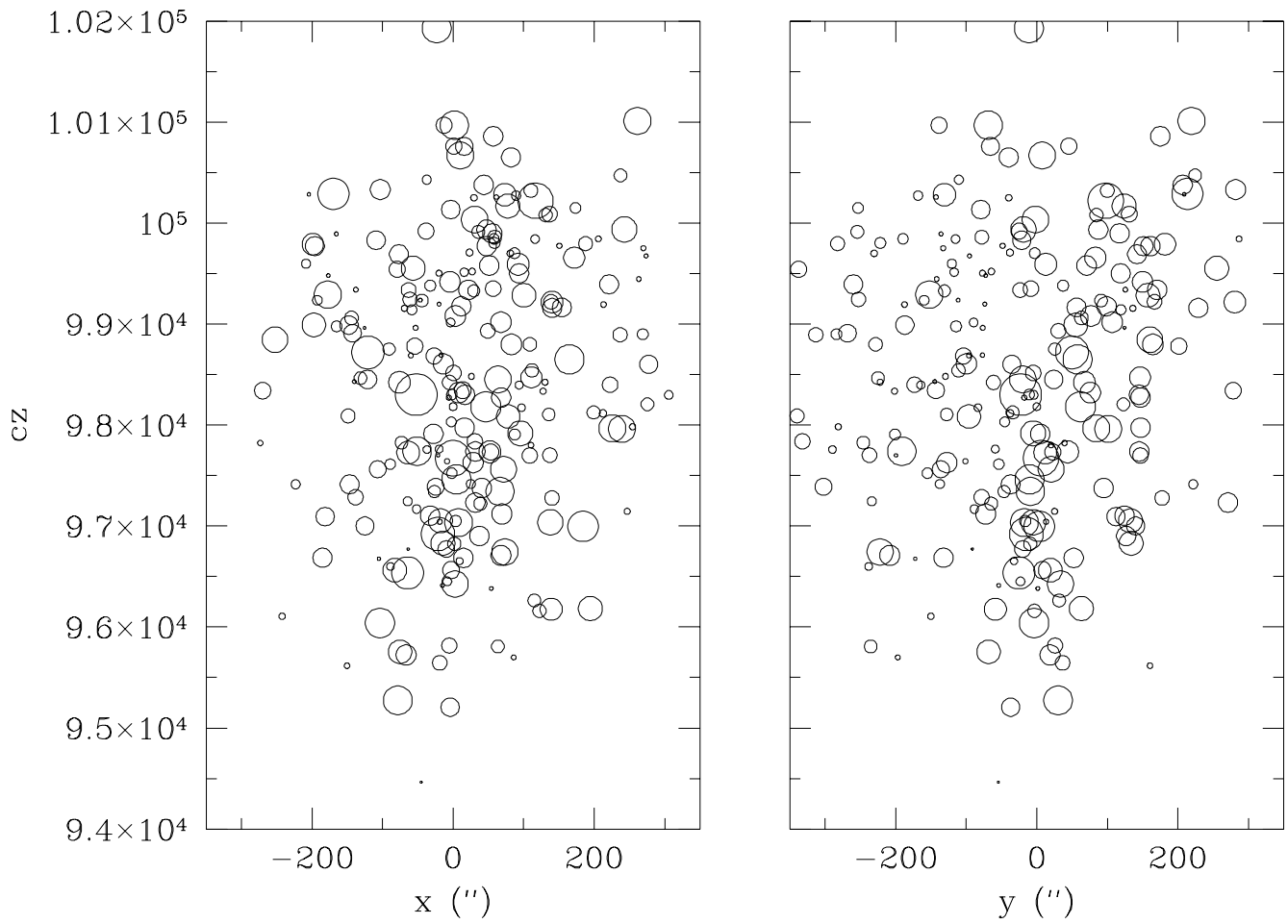
1.02×10⁵
1.01×10⁵
10⁵
9.9×10⁴
9.8×10⁴
9.7×10⁴
9.6×10⁴
9.5×10⁴
9.4×10⁴
cz
−200
0
200
x (″)
−200
0
200
y (″)

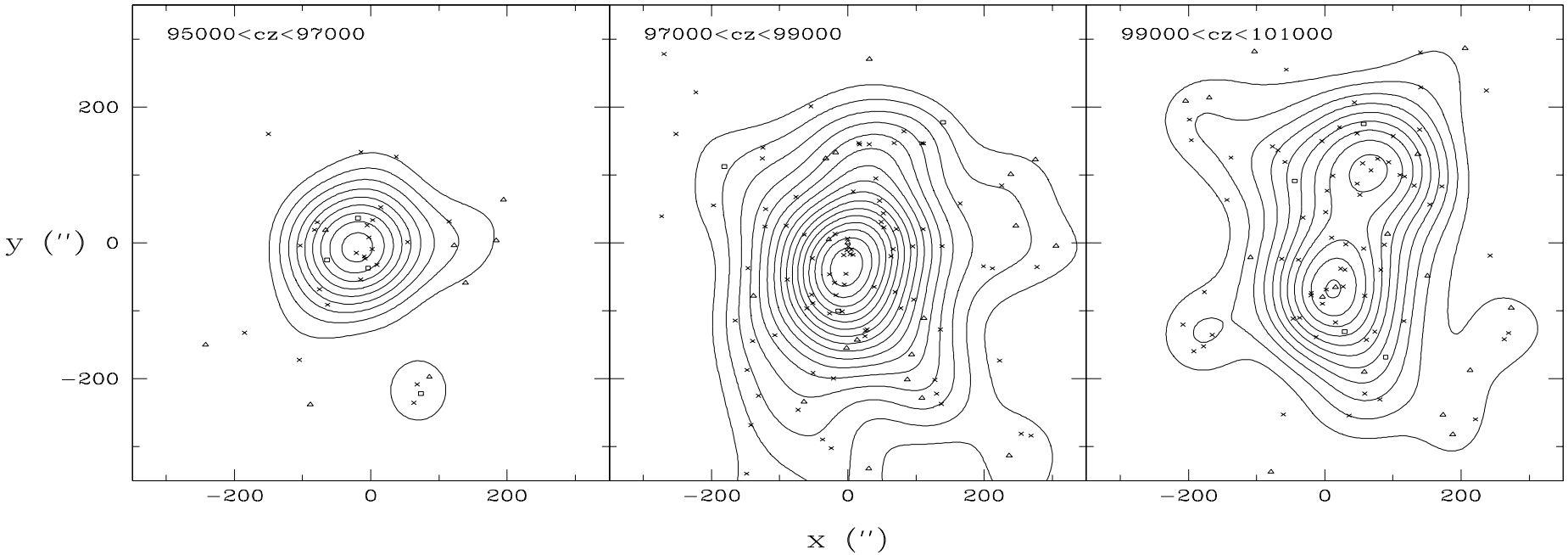
95000<cz<97000
97000<cz<99000
99000<cz<101000
200
0
−200
y (″)
−200
0
200
x (″)